

**Prediction of Local Convection and Land-Sea Breeze
Circulation over Taiwan**

Ying-Hwa Kuo

National Center for Atmospheric Research

P.O. Box 3000, Boulder, CO 80307, U.S.A.

Project Period: 1 July 1992 to 30 June 1993

A research report submitted to the
Central Weather Bureau
Ministry of Communications
Republic of China

June 4, 1993

1. Introduction

This report summarizes the work performed during the period of July 1 1992 to June 30 1993 under the Central Weather Bureau's project, entitled "Parameterization of boundary processes and simulations of local circulation in Taiwan." The objective of this project is to understand the local circulation over Taiwan, the convection due to local circulation, and the impact of boundary-layer and surface parameterization on the simulation of these circulation systems. For the first year of the two-year project, we focused on the simulation of the land-sea breeze circulation and the associated precipitation over Taiwan using the NCAR/Penn State nonhydrostatic mesoscale model version V (MM5). During the second year we will examine the impact of PBL and surface parameterization.

2. Mesoscale model and experiment design

The nonhydrostatic mesoscale model used in this study is described in Dudhia (1993). The vertical coordinate is $\sigma = (p_r - p_t)/(p_{s0} - p_t)$, where p_r is reference pressure, p_{s0} is surface pressure, and p_t is the constant pressure at the top of the model (100 mb). It is important to note that for the nonhydrostatic model the p_{s0} is obtained from a reference atmosphere, and it is held constant during the entire simulation. Pressure at a given grid point is defined as $p = p_r + p'$, where p' is a predictive variable. Given the fact that the reference atmosphere is not changing, this is equivalent of having a height coordinate that follows the terrain. For all the experiments performed in this study, the number of σ levels is 24 (0.0, 0.05, 0.10, 0.15, 0.20, 0.25, 0.30, 0.35, 0.40, 0.45, 0.50, 0.55, 0.60, 0.65, 0.70,

0.75, 0.80, 0.85, 0.89, 0.93, 0.96, 0.98, 0.99, 1.00), which gives 23 layers of unequal thickness at which the temperature, moisture, and wind components are defined. The computational domain contains an array of 67 x 67 grid points, centered at 24°N, 121°E, spaced 18 km apart for most of the experiments. In one simulation, a 6-km nested grid is activated to examine the impact of resolution on the simulation of local circulation.

The model's hydrological cycle includes explicit prediction of cloud water, rain water, ice and snow for the resolvable scale precipitation and the cumulus parameterization developed by Grell (1993) for subgrid scale precipitation. The parameterization of the surface-layer and planetary boundary-layer (PBL) was originally developed by Blackadar (1979). In this scheme, vertical fluxes of heat, moisture, and momentum are calculated explicitly between layers. Under stable conditions, the turbulent fluxes are parameterized by a local Richardson number. Under unstable regimes, vertical fluxes are modeled by mixing convective eddies originating at the surface with the environmental air in the PBL. Over the ocean, the sea surface temperature is held constant. The surface sensible and latent heat fluxes are formulated as functions of surface wind speed and stability parameters. In MM5, the surface parameters are specified based on a land-use look-up table. In this study, the land-use of Taiwan is specified as tropical or subtropical forest, which has a surface albedo of 12%, moisture availability of 50%, and roughness length of 50 cm.

The model is initialized with homogeneous fields derived from a single sounding. In this study, we use the Taipei sounding at 0000

UTC 19 June (TAMEX IOP11 as the initial condition) for most of the experiments (Fig. 1a). The Taipei sounding at 0000 UTC 2 June (Fig. 1b) is also used to test the impact of sounding structure and atmospheric stability on the land-sea breeze circulation. The model is initialized with calm wind, and it is integrated for 24 h.

To isolate the effect of Taiwan's local circulation, we eliminate the land mass over main land China and fill it with ocean. Therefore, Taiwan and its orography is the only land mass over the entire model domain. The terrain analysis is obtained by interpolating the 1-km Taiwan's orography to the model grid. Figure 2 shows the model terrain at 18 km and 6 km. With 18-km resolution, the two peaks of the Central Mountain Range (CMR) are 2228 and 2169 m, respectively. These are increased to 2709 and 2770 m with the use of the 6 km grid. The high-resolution grid also gives a considerably more details in the Taiwan's orography. For example, the strip of plains over southeastern China, not captured in the 18-km model, is retained in the 6-km model.

Table 1 summarizes the eight numerical experiments performed using the MM5 model. The first seven experiments use a uniform grid of 18 km. The last experiment uses a 18-km/6-km nested grid. The CNTL experiment includes surface energy fluxes, complete hydrological cycle, and the Taiwan's orography. To test the effect of latent heat release, we perform experiment NLHT in which the heating and cooling associated with condensation and evaporation are ignored. To examine the impact of CMR on the local circulation over Taiwan, we set the terrain height to zero in experiment NTER.

In experiment DRY, we initialize the model with identical temperature sounding as the control, however, the relative humidity is reduced by half of that of the original sounding. In this experiment we test the impact of the initial atmospheric water vapor on the land-sea breeze circulation. As a further test of the impact of the sounding structure, we initialize the model with the Taipei sounding at 0000 UTC 2 June in experiment IOP6.

In experiment RAD we add a simple atmospheric radiation parameterization to the model. The atmospheric long-wave radiative cooling, not included in the description by Anthes et al. (1987), follows the simple scheme of Paltridge and Platt (1976),

$$\frac{\partial T}{\partial t} = -(0.017T + 1.8) \quad (1)$$

where T is in $^{\circ}\text{C}$. This experiment serves as a benchmark for future experiment that will utilize a considerably more sophisticated scheme. In experiment NCRI, the cloud-radiation interaction processes included in the surface energy budget of the model is removed. Experiment M18/6 utilizes the same model physical parameterization as that of NCRI but with a nested 6-km grid.

3. Results of numerical experiments

a. Control simulation

Figure 3 shows the lowest level wind fields at 6-h intervals. Initialized with calm wind at 0000 UTC (0800 LST), the model has established a clearly defined sea-breeze within 6 h (1400 LST, Fig. 3a). In fact, the convergence pattern associated with the sea-breeze

is already visible by 3 h forecast (1100 LST, not shown). The maximum wind speed around the coast reaches 3.5 m s^{-1} . The highest speed takes place on the mountain top, in associated with mountain precipitation systems (to be shown later). A line of strong convergence is seen along the crest of the CMR, with maximum speed reaching 7.5 m s^{-1} . The sea-breeze reaches its maximum intensity at around 1700 LST (9 h forecast), producing maximum inflow of close to 5 m s^{-1} at places around the coast (Fig. 3b). By 2000 LST (12-h forecast) the convergent flow pattern associated with the sea breeze has changed into the diffluent pattern of the land-breeze (Fig. 3c). Wind everywhere around the coast is very light (less than 0.5 m s^{-1}), except near the southwestern coast (which is associated with the outflow of a convective system). Wind on top of the CMR remains strong, reaching 15 m s^{-1} at places. As will be shown later, these are largely related to the precipitation systems on the mountain top. The light land-breeze persists through the night as shown by the wind at 0500 LST (21-h forecast, Fig. 3d).

Figure 4 shows the lowest level temperature at 6 h intervals. At the initial time the temperature is specified as a function of the terrain height. The temperature over the ocean is 26.4°C , and it drops to 16.3°C at the peak of the CMR (Fig. 4a). With solar heating, the temperature over the southwestern plain of Taiwan rises to 28.5°C and 17.2°C over the peak of CMR (Fig. 4b). The highest land-sea temperature contrast occurs on the southwestern plain of Taiwan, with a value of about 2.5°C . By 2000 LST temperature drops over most of the island. Except for the northwestern coast and the eastern coast, the land temperature is colder than the ocean

temperature. Over the northwestern coast, the temperature contrast has dropped to 1.3°C. The warm pocket of air in the vicinity of Hwalien appears to be caused by persistent down-slope flow associated with the land-breeze and the steep orography over the region.

The model produced 3-h accumulated total rainfall and convective rainfall are shown in Figs. 5 and 6, respectively. At 1400 LST light convective precipitation occurs over the northern mountain area and the southwestern coast, with 3-h amount of 0.5 cm. No grid-point resolvable-scale rainfall is generated. By 1700 LST (not shown), significant amount of precipitation takes place along the peaks of the CMR, with maximum 3-h rainfall reaching 3.5 cm. A major portion of this is the grid-resolvable rainfall. The precipitation system near Kaoshiung remains to be convective and the amount has increased to 1.9 cm. By 2000 LST the mountain precipitation continues to increase, the peak 3-h rainfall now reaching 5.1 cm. The convective rainfall over Kaoshiung also has increased to 3.4 cm. As the daily solar heating ceases, the rainfall also decreases. By 2300 LST only scattered convective showers are predicted over the mountain tops (not shown). Three hours later, we find the rainfall area has shifted to the eastern slope of the CMR, with peak 3-h rainfall of 1.3 cm (Fig. 5c). Most of the rainfall is produced by the subgrid scale convective parameterization (see Fig. 6c). The precipitation amount continues to decrease, and by 0800 LST rainfall again starts over the mountain top as a new day of diurnal heating cycle begins.

In summary, we find that the MMS model has successfully simulated the land-sea breeze over Taiwan and its associated

precipitation during the Mei-Yu period. The simulated sea-breeze has a maximum wind speed of 5 m s^{-1} , and that of the land breeze is about 1 m s^{-1} . We also find that the air flow and temperature prediction to be strongly affected by the precipitation over the top of the CMR.

b. Effect of latent heat release

With the removal of latent heating, the convergence associated with the day-time sea-breeze is considerably weakened. Notice that the $3\text{-}5 \text{ m s}^{-1}$ sea-breeze off the west coast at 1700 LST (9 h forecast, Fig. 7a) is not visible in the NLHT experiment. Apparently, the latent heat release associated with the resolvable-scale precipitation over the mountain is important in inducing additional low-level convergence. Also, without latent heating the maximum wind speed on the mountain top does not exceed 7.5 m s^{-1} . At 0500 LST (Fig. 7b), weak land-breeze is established similar to that of CNTL. The only visible difference is the absence of the strong outflow (15 m s^{-1}) in NLHT, which was seen in the CNTL.

With the removal of latent heat release, the cooling associated with the rain drop evaporation and ice and snow melting will also be ignored. Figure 8 compares the surface temperature at 1700 LST (9-h forecast) and 0500 LST (21-h forecast) between CNTL and NLHT. We note that the temperature over the island is generally higher for the NLHT run at 1700 LST. The main reason is the lack of evaporative cooling. Also, the temperature distribution in NLHT mimics that of terrain, while that in CNTL does not show the same degree of agreement. This again indicates that the downdrafts cooling associated with precipitation is an important forcing for the local

circulation in Taiwan. Early in the morning (0500 LST, 21-h forecast), the temperatures between the two experiments become more similar because precipitation has subsided in CNTL.

c. Effect of sounding structure

To examine the effect of initial moisture structure on the simulation of land-sea breeze and its associated precipitation, we reduce the relative humidity in the sounding by half in experiment DRY. The resulting dew point temperature is shown as a dashed line in Fig. 1a. With a 50% reduction of relative humidity, one major difference is the resulting precipitation. The maximum 12-h day time precipitation for CNTL over the mountain top is 9.04 cm, while the corresponding amount in DRY was only 0.037 cm. The difference is two-order of magnitude. It is clear that the moisture content in a given sounding is crucial in determining the precipitation associated with the land-sea breeze.

With virtually no precipitation in the DRY experiment, the surface heating is not affected by evaporative cooling. Consequently, the surface temperature is warmer in DRY as compared with that of CNTL, and the resulting sea-breeze becomes stronger. Figure 9 shows the lowest level wind and temperature at 1400 LST (6-h forecast) for DRY. The temperature over the southwestern plains reaches as high as 30.2°C, while the corresponding temperature in CNTL is 28.5°C. The corresponding sea-breeze off the coast near Kaoshiung is 5.0 m s⁻¹ in Dry, and 3.2 m s⁻¹ in CNTL. These results show that evaporative cooling and convective downdrafts associated with sea-breeze convection has a profound influence on the surface temperature and the evolution of the sea-breeze flow.

To test the sensitivity of the sea-breeze circulation to differences in sounding structure, we run experiment IOP6 using the Taipei sounding at 0000 UTC 2 June as the initial condition. A comparison between IOP11 sounding versus the IOP6 sounding shows that there is an inversion layer between 900 and 950 mb in the IOP11 sounding. Also, the entire sounding is warmer, and has higher moisture contents. The low-level inversion in the IOP6 sounding is not as strong.

Overall speaking, the surface temperature is about 1-2°C cooler in the IOP6 simulation as compared with CNTL, which is to a large degree due to lower initial temperature in IOP6. However, the sea-breeze depends on the land-ocean temperature difference, rather than the absolute temperature. We find that the sea-breeze flow in IOP6 to be quite comparable with that of CNTL (see Fig. 10). A major difference occurs in the accumulated 12-h precipitation. Figure 11 compares the 12-h accumulated precipitation between CNTL and IOP6. The day-time mountain top precipitation is quite similar between CNTL and IOP6, except that heavier amount is predicted in CNTL. Moreover, the rainfall over the southwestern coast of Taiwan (near Kaoshiung) is not predicted based on the IOP6 sounding. Since the precipitation over that area is entirely produced by the Grell scheme, which is derived originally from the Arakawa-Schubert (1974) scheme, this might be related to the amount of large-scale destabilization experienced in that area. A detailed analysis is needed to understand this difference in convective rainfall prediction.

d. Effect of the Central Mountain Range

With the Central Mountain Range sitting in the middle of Taiwan island, it can exert a significant amount of forcing on the flow in the vicinity of Taiwan. Even in a simulation without mean flow, the mountain can act as an elevated heat source, significantly affecting the temperature structure over the entire island and the land-sea breeze circulation. In order to better understand the effect of CMR, we perform an experiment NTER in which the terrain height is set to zero over the entire model domain. Without CMR, the model produces an organized sea-breeze, which moves steadily from the coast into Taiwan. The sea-breezes from the east and west coasts eventually collide with one another between 1700 and 2000 LST, and produce precipitation right over the central portion of Taiwan. The maximum sea-breeze has a speed of 3.5 m s^{-1} , and the maximum land-breeze reaches around 1 m s^{-1} (See Fig. 12).

The temperature prediction during the day-time is fairly reasonable. The maximum inland temperature increases steadily from 26.4°C at 0800 LST (0-h forecast) to 29.1°C at 1700 LST (9-h forecast). After precipitation taking place over the central strip of Taiwan, downdrafts and evaporative cooling brings the temperature down to 23.6°C , while the remaining part of Taiwan is having a temperature of 27.6°C . By 0500 LST (21-h forecast), the inland temperature has been cooled to 26.9°C , approximately 1°C cooler than the ocean. The much larger day-time land-ocean temperature contrast as compared with the night-time ocean-land temperature difference explains the much stronger sea-breeze than the land breeze (see Fig. 13).

The 12-h accumulated rainfall for NTER is shown in Fig. 14. The day-time accumulated precipitation has a maximum value of 0.76 cm, approximately 10% of that in the CNTL. The night-time rainfall for NTER is even smaller, reaching a maximum of 0.1 cm. It is clear that the CMR has played an extremely important role in enhancing the sea-breeze circulation and the associated precipitation.

e. Effect of radiation

In all the previous simulations, no atmospheric long wave radiation is included. In order to provide an estimate of radiative cooling effects, we include the simple radiative cooling scheme of Paltridge and Platt (1976) in experiment RAD.

A comparison between CNTL and RAD shows that the land-sea breeze circulation between these two experiments are highly similarly. Therefore, it is not repeated here. Obviously with added radiative cooling, the atmospheric temperature is gradually cooled. For example, the temperature over the southwestern plain has a maximum temperature of 27.8°C at 1400 LST (6-h forecast, Fig. 15a), 0.7°C cooler than that in CNTL. By 0200 LST (18-h forecast, Fig. 15b), this temperature difference has increased to 1.3°C.

Perhaps, the most interesting difference lies in the precipitation forecast. During the day-time, the accumulated precipitation in RAD (Fig. 16a) has a pattern very similar to that of CNTL over the mountain, except that the amounts are in general larger than those of CNTL. The main difference is that more convective precipitation is produced around the coast. This situation is even more apparent during the night-time: CNTL produces basically no coastal precipitation while RAD produces moderate

convective precipitation over the west coast (Fig. 16b). The enhanced night-time precipitation near the coast is consistent with many observational studies (Chen and Yan 1988; Bresch and Johnson 1990). The coastal precipitation is entirely produced by the Grell cumulus parameterization. The explicit scheme has no contribution here. It appears that atmospheric radiative cooling is important in destabilizing the coastal atmosphere, and stimulating convective precipitation over the coastal region. The effect is particularly effective during the night. Further study using a more sophisticated radiation scheme should be attempted in the future.

f. Effect of cloud-radiation interaction

When clouds are present, they would affect both the short-wave and long wave radiation, which will in turn, affect the ground temperature calculation based on the surface energy budget. In MM5, a simple scheme based on Benjamin (1983) is used to simulate this cloud-radiation interaction process. In all the aforementioned numerical experiments, this effect is included in the model. In NCRI experiment, we turn off this interactive process to study its impact on land-sea breeze simulation. Figure 17 shows the surface temperature prediction by NCRI at 1400 LST (6-h forecast, Fig. 17a) and 0200 LST (18-h forecast, Fig. 17b). Compared with the results of RAD (Fig. 15), we see that the day-time temperature over the southwestern coast is up to 1.4°C warmer in the experiment without cloud radiation interaction. This is due to the fact that solar radiation is not blocked by the cloud, and a warmer ground temperature is produced. In the early morning hours, this difference in the surface

temperature prediction is considerably reduced (maximum value of 0.4°C).

Without cloud-radiation interaction, the mountain becomes an even more effective elevated heat source. As a result, the day-time precipitation in NCRI is considerably larger than that in RAD (compare Fig. 18a with Fig. 16a). For example, the peak rainfall amount over northern CMR is 7.8 cm in RAD and 13.4 cm in NCRI. Also, the day-time convective precipitation near Kaoshiung is moved further inland. The precipitation amount over the mountain falls sharply during the night in NCRI. The prediction of coastal rainfall at night is still captured in NCRI, however. This might be a result of precipitation dry out (depletion of the atmospheric water vapor during the day). All these results point to the conclusion that a considerably stronger sea-breeze is developed during the day in NCRI, which becomes obviously in a comparison of surface wind between NCRI and RAD at 1400 LST (6-h forecast, Fig. 19).

g. Effect of horizontal resolution

With the use of 6-km horizontal resolution, the CMR is resolved better, and the surface air temperature prediction looks even more realistic. Figure 20 shows the lowest level temperature for M18/6 experiment at 6 h intervals. At the initial time, the temperature over the peak of CMR is 12.8°C, compared with 16.7°C for the 18-km model. The temperature gradient also more faithfully reflects the actual temperature observations due to terrain variation. By 1400 LST (6-h forecast), the temperature over the southwestern plains has risen to 30.4°C, very comparable with the actual observations in TAMEX IOP11. The temperature in the Taipei basin also reaches

29.4°C. Realistic cooling is also simulated during the night as seen in the temperature prediction at 2000 LST (12-h forecast) and 0200 LST (18-h forecast). These results again illustrate the importance of having a good horizontal model grid resolution in predicting local circulation over Taiwan.

With a 6-km grid resolution, we can now begin to see the separation between the sea breeze and the mountain-valley circulation at 3-h forecast (1100 LST, Fig. 21a), which is indicated by a surge of higher speed wind at the coast, a zone of weaker wind further inland, and again stronger wind surrounding the mountains. The sea-breeze later moves inland and joins force with the mountain-valley circulation to stimulate precipitation over the mountains (1400 LST, Fig. 21b). The M18/6 experiment also simulates extremely well the transition from sea-breeze into land-breeze as shown by the surface wind fields at 2000 LST (12-h forecast, Fig. 21c) and 0200 LST (18-h forecast, Fig. 21d).

The 12-h accumulated rainfall is shown in Fig. 22. Compared with the prediction of NCRI, which uses the same physical parameterization as M18/6, the rainfall distribution in the 6-km model shows considerably more mesoscale details. During the day-time heavy precipitation is predicted over the CMR, with very heavy amounts at the foothills of CMR as well (places like Chia-Yi). During the night, heavy precipitation has shifted to the coastal region, with amount reaching 5 cm in 12 hour. Overall speaking, the use of the 6-km model leads to heavier rainfall amount and more realistic rainfall distribution.

4. Summary and conclusions

We have performed a series of 8 numerical experiments using the nonhydrostatic MM5 model. The results show that the control experiment is capable of simulating realistic land-sea breeze and mountain-valley circulation. The variation of precipitation through the diurnal cycle is also consistent with the available observations. Further sensitivity experiments lead to the following conclusions:

- a. The precipitation due to local circulation is highly sensitive to the sounding structure. For example, reducing the atmospheric moisture content by half, almost entirely eliminates the precipitation. Also, using IOP6 sounding versus IOP11 sounding to initialize the model also leads to significant differences in rainfall amount and distribution. This clearly illustrates the complexity in predicting afternoon thunderstorms due to land-sea breeze over Taiwan.
- b. The Central Mountain Range is a preferred location for local circulation. This is because the mountains also act as an elevated heat source. The stimulation of precipitation due to mountain valley circulation, and later aided by sea-breeze circulation often leads to significant day-time precipitation over the mountain. Precipitation over the mountain subsides significantly during the night, due to both nocturnal cooling and precipitation evaporation cooling.
- c. The latent heating due to mountain top precipitation and cooling due to rain drop evaporation have a significant impact on the local circulation in Taiwan. The latent heating tends to produce strong rising motion over the mountains, and

- strengthens the sea-breeze. The evaporative cooling tends to cool the lower troposphere, enhancing the land-breeze and the mountain-breeze.
- d. When the Central Mountain Range is removed from the model terrain field, a much simpler land-sea breeze circulation develops. Also, the precipitation is less than 10% of the case with the CMR. These results indicate that the mountain-valley circulation is of equal importance, if not more, to the land-sea breeze circulation in producing local precipitation over Taiwan.
 - e. Both the atmospheric long-wave radiation cooling and the cloud-radiation interaction have a profound influence on the precipitation distribution, although they don't alter the basic land-sea breeze and mountain-valley circulation. The atmospheric radiation cooling leads to stronger destabilization near the coastal area and strengthens the night-time precipitation over the coastal region. The cloud-radiation interaction is essential in getting a more realistic temperature prediction. When this effect is removed, the model produces an overly strong mountain-valley circulation and excessive day-time precipitation. As a result, the night-time precipitation over the mountains is significantly reduced.
 - f. The use of 6-km grid resolution leads to a much better definition of the Central Mountain Range, and better surface temperature prediction. Consequently, the rainfall distribution also shows a more realistic mesoscale pattern. A 6-km resolution is needed to see the separation of sea-breeze from the mountain-valley circulation. A more realistic night-time

convective precipitation near the coast is simulated with an improved horizontal resolution.

References:

- Anthes, R. A., R.-Y. Hsieh, and Y.-H. Kuo, 1987: Description of the Penn State/NCAR Mesoscale Model Version 4 (MM4). NCAR Tech. Note, NCAR/TN-282+STR, 66 pp.
- Arakawa, A., and W. H. Schubert, 1974: Interaction of a cumulus cloud ensemble with the large scale environment, Part I. *J. Atmos. Sci.*, **31**, 674-701.
- Benjamin, S. G., 1983: *Some Effects of Surface Heating and Topography on the Regional Severe Storm Environment*. Ph.D. thesis, Department of Meteorology, The Pennsylvania State University, 265 pp.
- Blackadar, A. K., 1979: High resolution models of the planetary boundary layer. *Advances in Environmental Science and Engineering*, J. R. Pfafflin and E. N. Zeigler, Eds., Gordon and Breach, 50-85.
- Bresch, J. F., and R. H. Johnson, 1990: Rainfall and vertical motion associated with TAMEX precipitation systems. *Proceedings, Workshop on TAMEX Scientific Results*, 24-26 Sep. 1990, Boulder, CO, 84-89.
- Chen, G. T.-J., and J. S. Yang, 1988: Climatological aspects of convective rainfall over Taiwan area in Mei-Yu season. *Proceedings, Conference on Weather Analysis and Forecasting*, Central Weather Bureau, Taipei, 565-571.

- Dudhia, J. , 1993: A nonhydrostatic version of the Penn State-NCAR mesoscale model: Validation tests and simulation of an Atlantic cyclone and cold front. *Mon. Wea. Rev.*, **121**, 1493-1513.
- Grell, G. A., 1993: Prognostic evaluation of assumptions used by cumulus parameterizations. *Mon. Wea. Rev.*, **121**, 764-787.
- Paltridge, G. W., and C. M. R., Platt, 1976: *Radiative processes in meteorology and climatology*. Elsevier, N.Y.

Figure Captions:

- Fig. 1 Sounding at Taipei for (a) 0000 UTC 19 June 1987 and (b) 0000 UTC 2 June 1987. The dashed line in (a) represents the reduced relative humidity used in experiment DRY.
- Fig. 2. The model terrain for (a) the 18-km model and (b) the 6-km model.
- Fig. 3. Lowest level wind at (a) 1400 LST (6-h forecast), (b) 1700 LST (9-h forecast), (c) 2000 LST (12-h forecast) and (d) 0500 LST (21-h forecast) for the control experiment (CNTL). The convention for the wind barb is half barb for 0.5 m s^{-1} , long barb for 1 m s^{-1} , flag for 5 m s^{-1} . This convention is used for the rest of the report.
- Fig. 4. Lowest level temperature at (a) 0800 (0-h forecast), (b) 1400 LST (6-h forecast), (c) 2000 LST (12-h forecast), and (d) 0200 LST (18-h forecast) for CNTL.
- Fig. 5. 3-h accumulated total rainfall valid at (a) 1400 LST (6-h forecast), 2000 LST (12-h forecast), (c) 0200 LST (18-h forecast), and (d) 0800 LST (24-h forecast) for CNTL.

- Fig. 6. 3-h accumulated convective rainfall valid at (a) 1400 LST (6-h forecast), 2000 LST (12-h forecast), (c) 0200 LST (18-h forecast), and (d) 0800 LST (24-h forecast) for CNTL.
- Fig. 7. Lowest level wind at (a) 1700 LST (9-h forecast) and (b) 0500 LST (21-h forecast) for NLHT.
- Fig. 8. Lower level temperature at (a) 1700 LST (9-h forecast) and (b) 0500 LST (21-h forecast) for CNTL, and (c) 1700 LST (9-h forecast) and (d) 0500 LST (21-h forecast) for NLHT.
- Fig. 9. Lowest level (a) wind and (b) temperature at 1400 LST (6-h forecast) for DRY.
- Fig. 10. Lowest level (a) wind and (b) temperature at 1400 LST (6-h forecast) for IOP6.
- Fig. 11. 12-h accumulated rainfall for (a) 0-12 h forecast, (b) 12-24 h forecast for CNTL, and (c) 0-12 h forecast, (d) 12-24 h forecast for IOP6.
- Fig. 12. Lowest level wind at (a) 1400 LST (6-h forecast), (b) 1700 LST (9-h forecast), (c) 2000 LST (12-h forecast) and (d) 0500 LST (21-h forecast) for the no-terrain experiment (NTER).
- Fig. 13. Lowest level temperature at (a) 1400 LST (6-h forecast), (b) 1700 LST (9-h forecast), (c) 2000 LST (12-h forecast) and (d) 0500 LST (21-h forecast) for the no-terrain experiment (NTER).
- Fig. 14. 12-h accumulated rainfall for (a) 0-12 h forecast, (b) 12-24 h forecast for NTER.
- Fig. 15. Lowest level temperature at (a) 1400 LST (6-h forecast) and (b) 0200 LST (18-h forecast) for RAD.
- Fig. 16. 12-h accumulated rainfall for (a) 0-12 h forecast, (b) 12-24 h forecast for RAD.

- Fig. 17. Lowest level temperature at (a) 1400 LST (6-h forecast) and (b) 0200 LST (18-h forecast) for NCRI.
- Fig. 18. 12-h accumulated rainfall for (a) 0-12 h forecast, (b) 12-24 h forecast for NCRI.
- Fig. 19. Lowest level wind field at 1400 LST (6-h forecast) for (a) RAD and (b) NCRI.
- Fig. 20. Lowest level temperature at (a) 0800 LST (0-h forecast), (b) 1400 LST (6-h forecast), (c) 2000 LST (12-h forecast) and 0200 LST (18-h forecast) for M18/6.
- Fig. 21. Lowest level wind fields at (a) 1100 LST (3-h forecast), (b) 1400 LST (6-h forecast), (c) 2000 LST (12-h forecast), and (d) 0200 LST (18-h forecast) for M18/6.
- Fig. 22. 12-h accumulated rainfall for (a) 0-12 h forecast, (b) 12-24 h forecast for M18/6.

Table 1 Summary of Numerical Experiments

Exp. name	Atm. radia.	Cloud radia.	Surface fluxes	Latent heating	Mount.
CNIL	no	yes	yes	yes	yes
NLHT	no	yes	yes	no	yes
DRY	no	yes	yes	yes	yes
IOP6	no	yes	yes	yes	yes
NTER	no	yes	yes	yes	no
RAD	yes	yes	yes	yes	yes
NCRI	yes	no	yes	yes	yes
M18/6	yes	no	yes	yes	yes

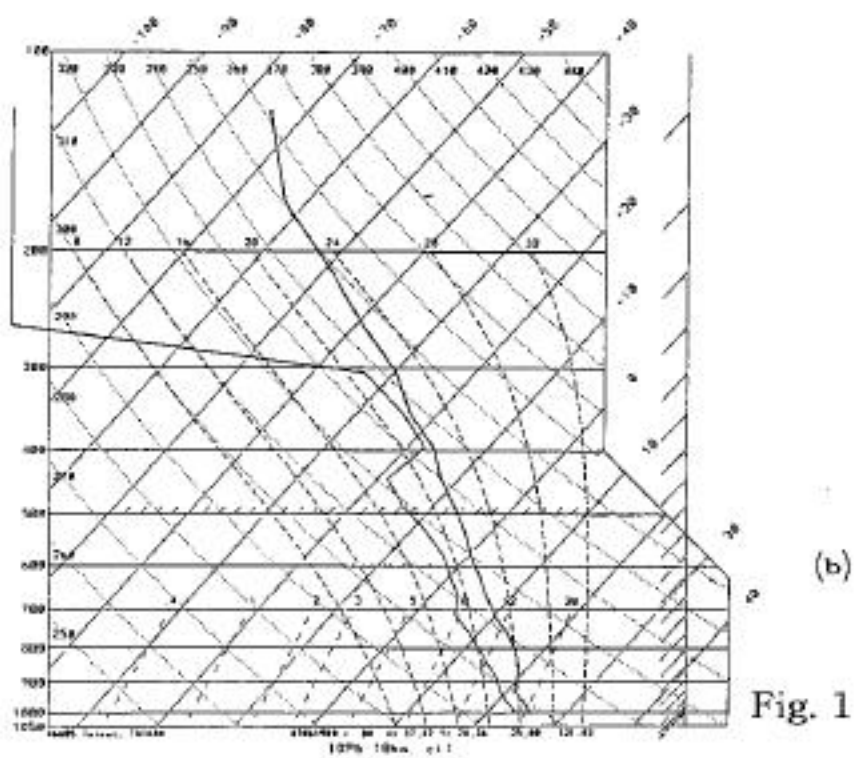
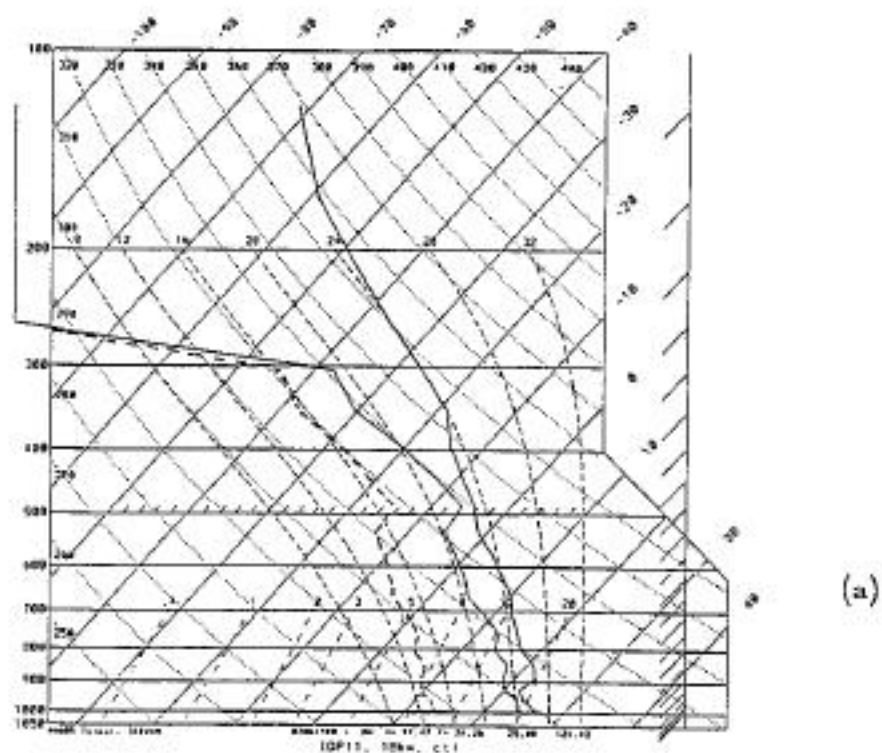


Fig. 1

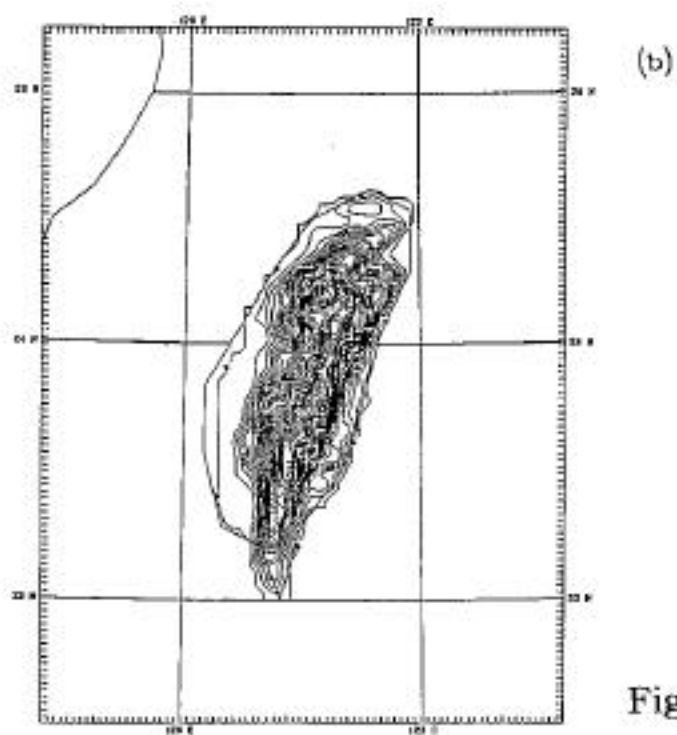
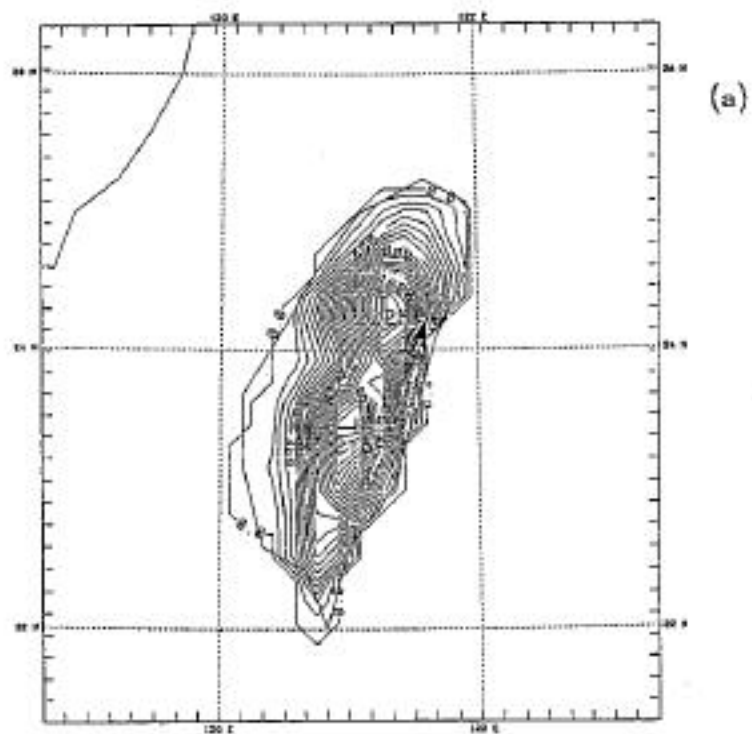


Fig. 2

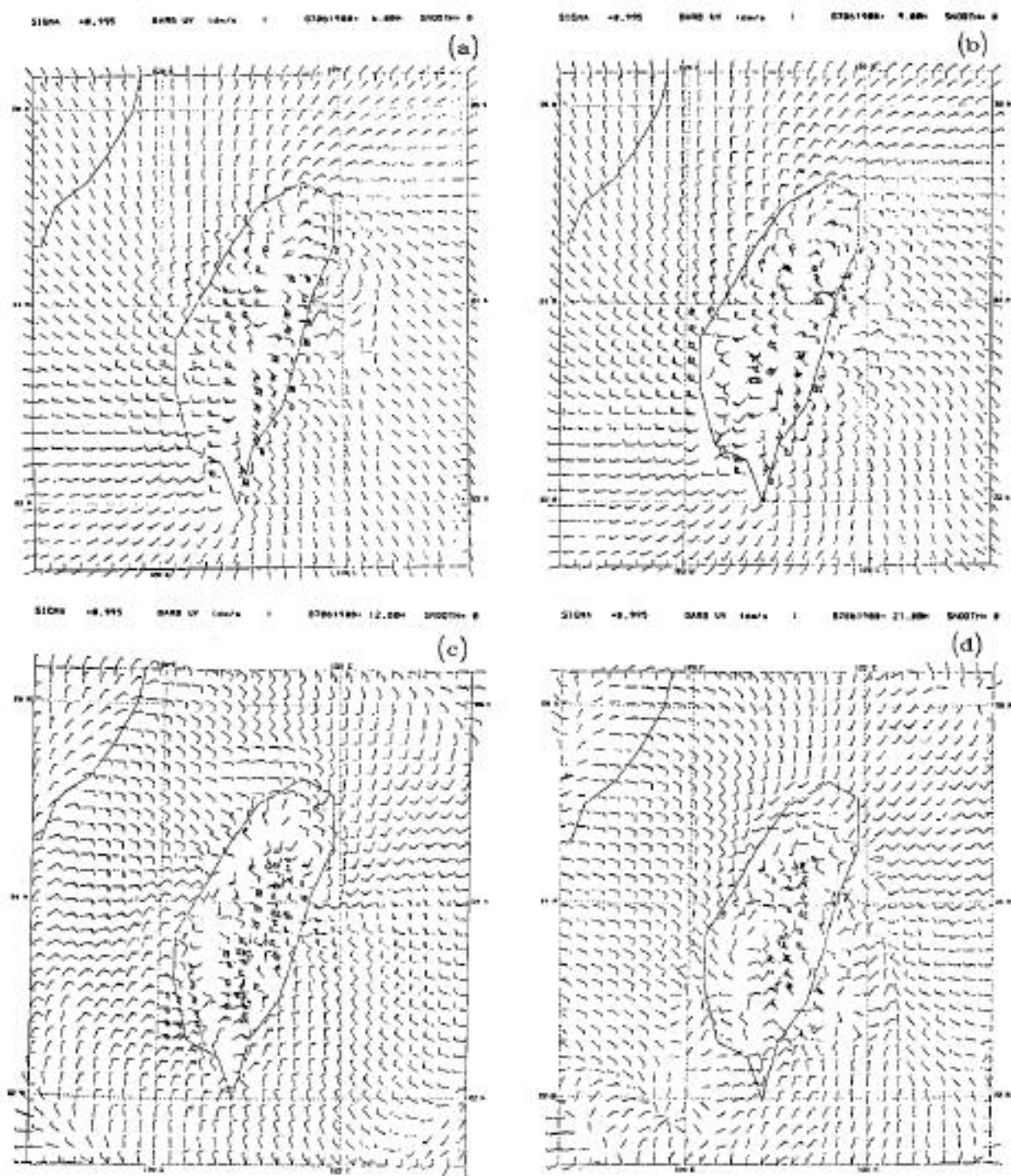


Fig. 3

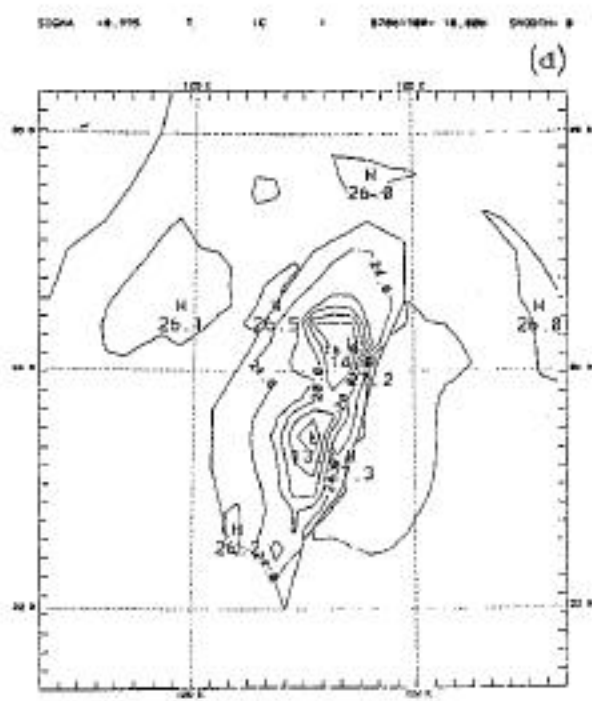
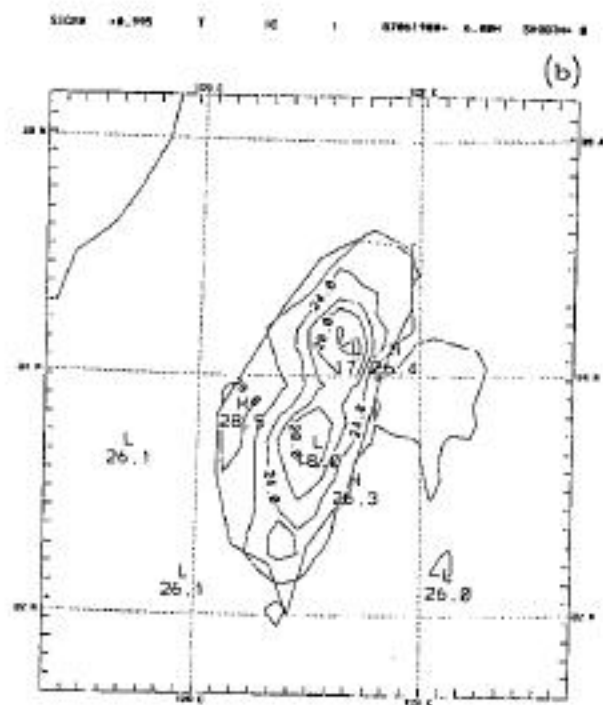
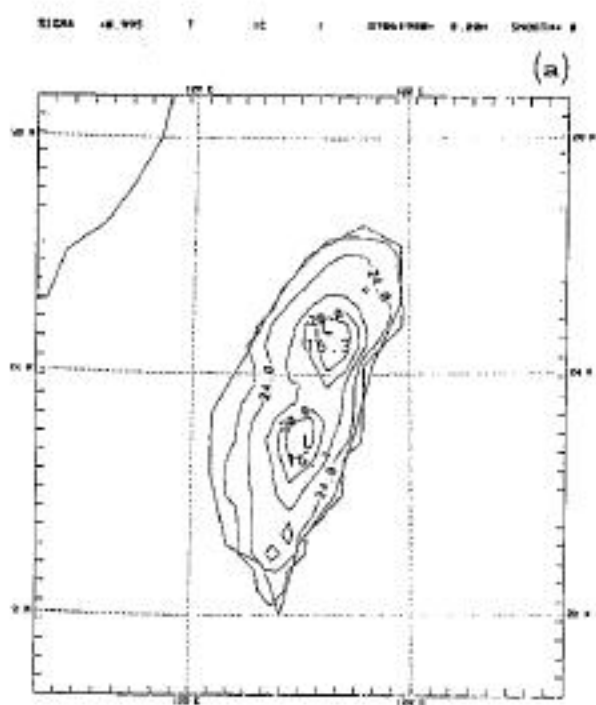


Fig. 4

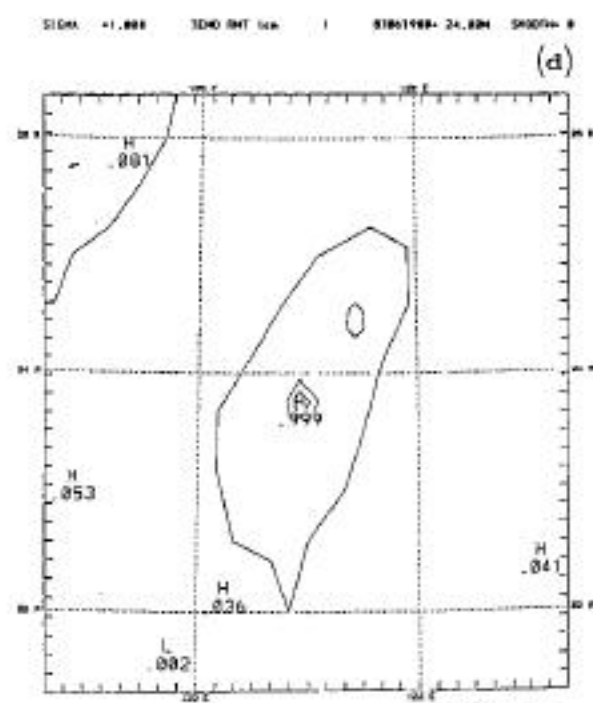
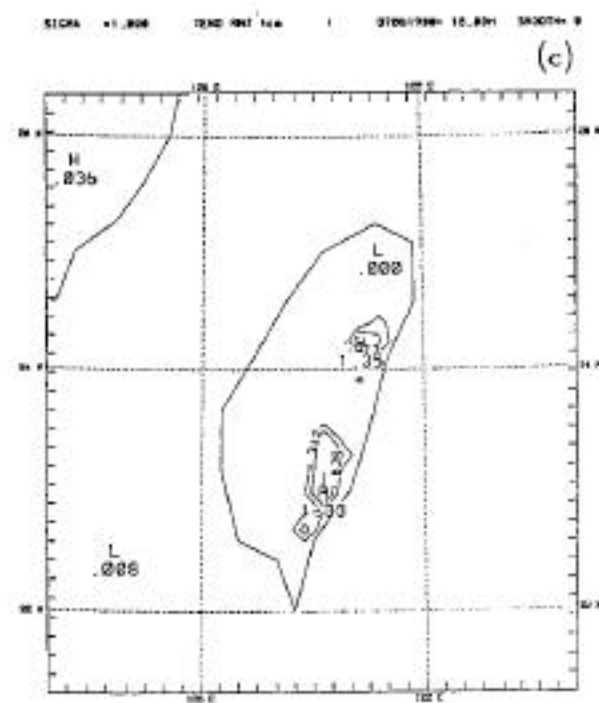
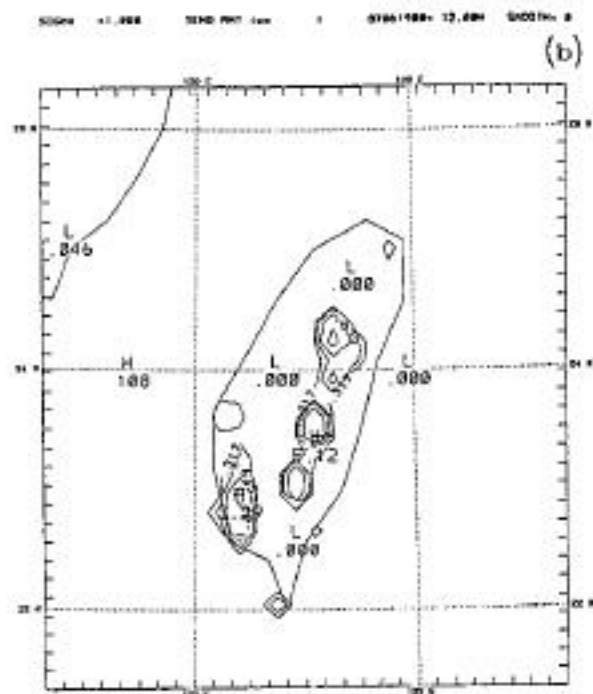
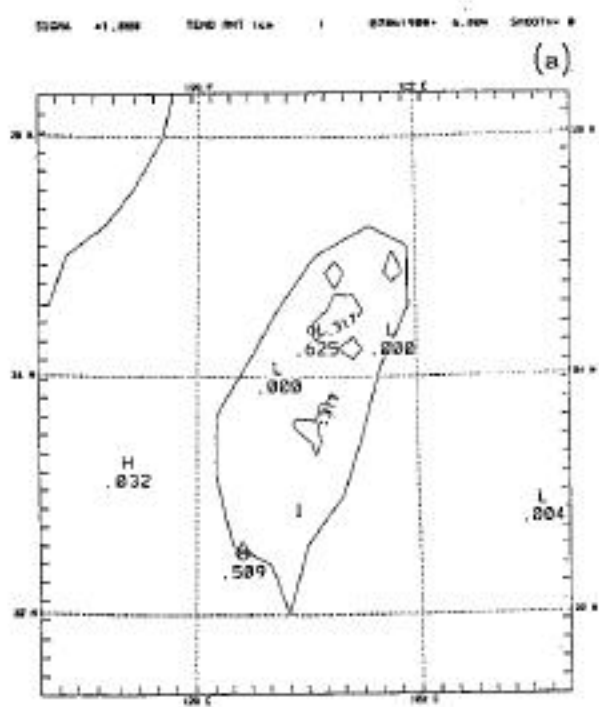
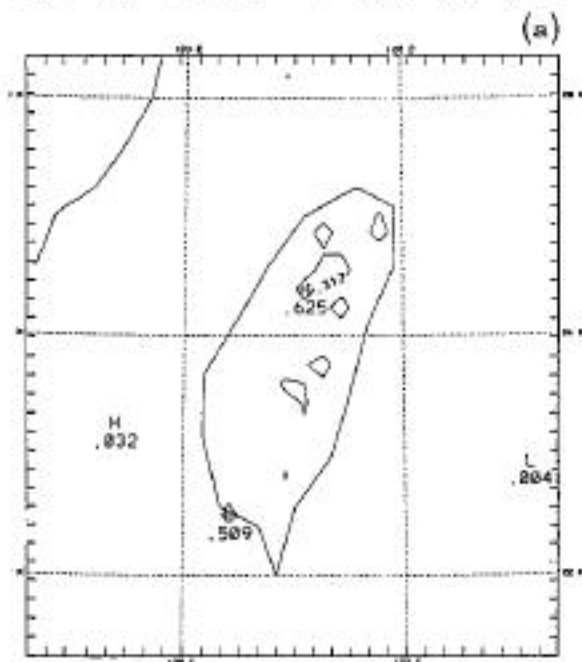
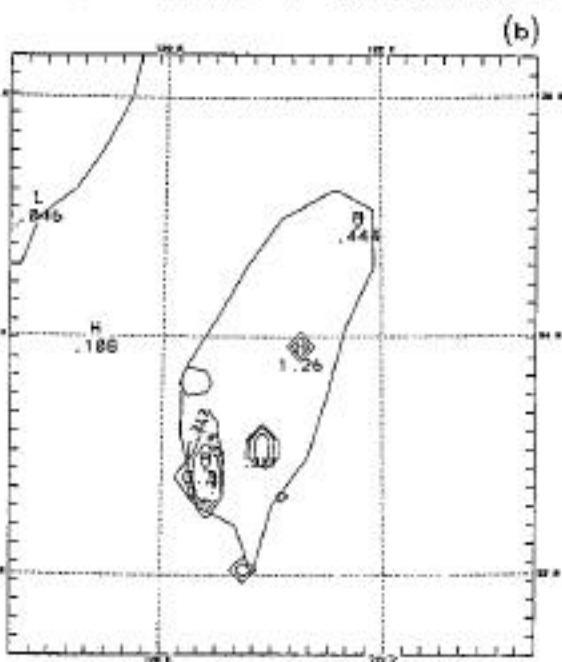


Fig. 5

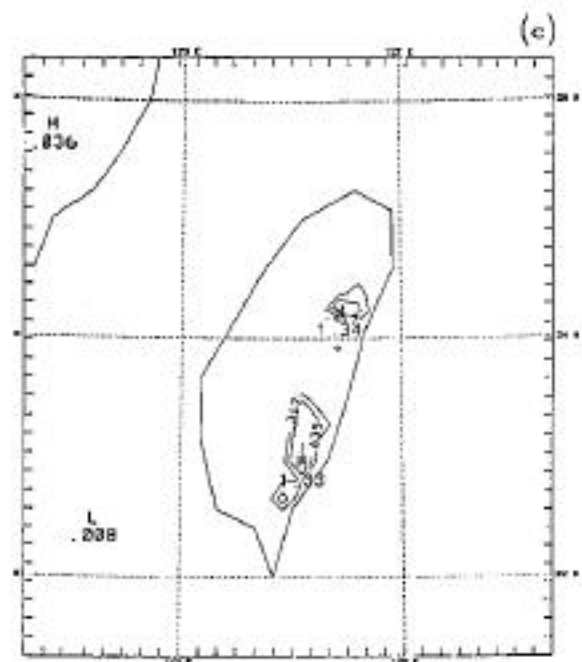
SIGMA =1.800 TEND PNC low I STAGE1999= 0.000 SMOOTHS= 0



SIGMA =1.800 TEND PNC low I STAGE1999= 12.000 SMOOTHS= 0



SIGMA =1.800 TEND PNC low I STAGE1999= 18.000 SMOOTHS= 0



SIGMA =1.800 TEND PNC low I STAGE1999= 24.000 SMOOTHS= 0

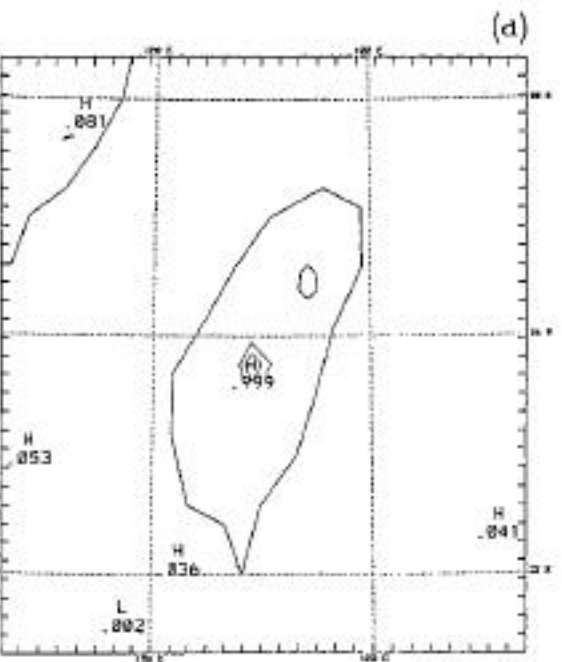
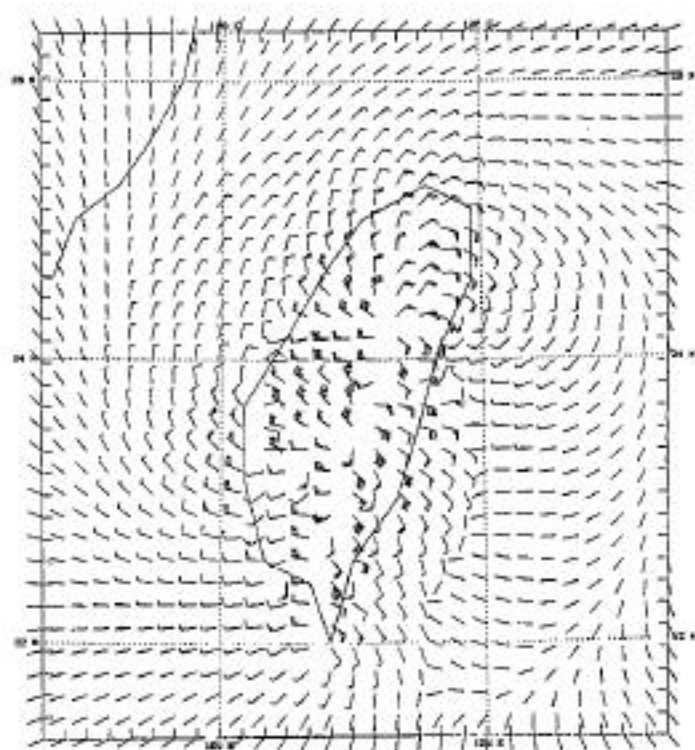


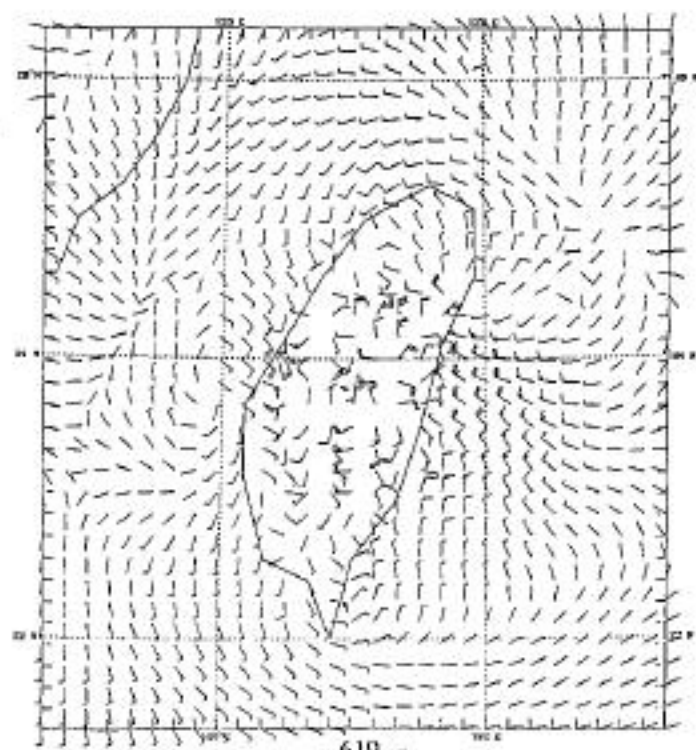
Fig. 6

SIGMA = 0.995 DARS UV km/s ? 07051920 = 1.020 SHOOTIN = 0



(a)

SIGMA = 0.995 DARS UV km/s ? 07051920 = 21.200 SHOOTIN = 0

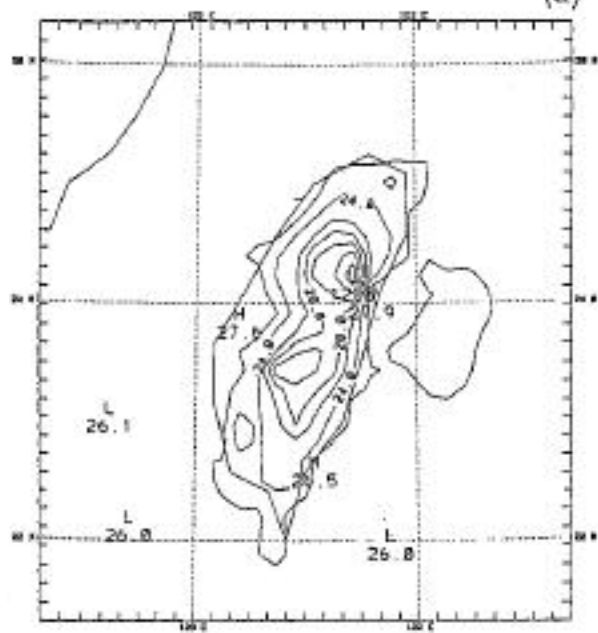


(b)

Fig. 7

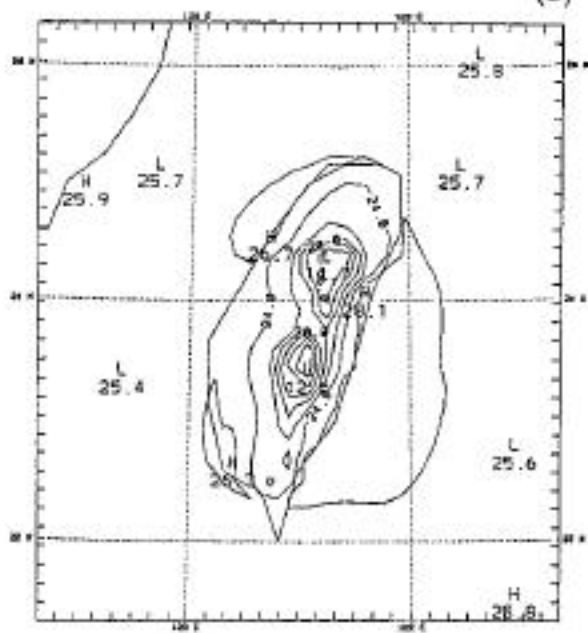
SIGMA = 0.195 T IC I DTBW1980 1.000 SHOOT= 0

(a)



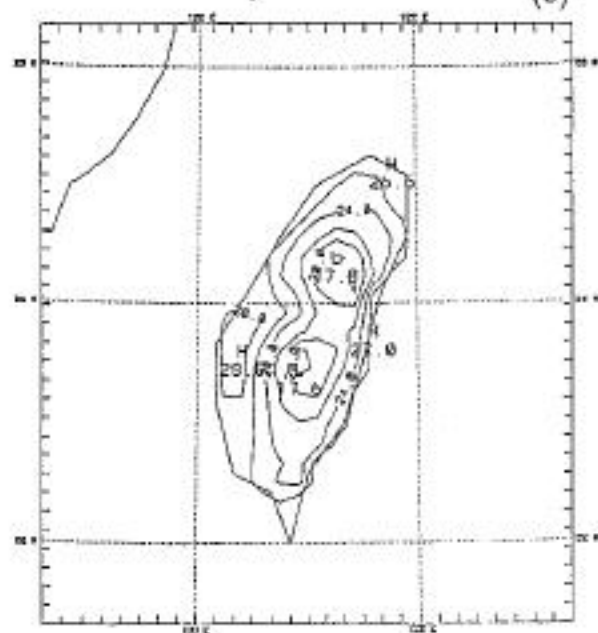
SIGMA = 0.195 T IC I DTBW1980 21.000 SHOOT= 0

(b)



SIGMA = 0.195 T IC I DTBW1980 1.000 SHOOT= 0

(c)



SIGMA = 0.195 T IC I DTBW1980 21.000 SHOOT= 0

(d)

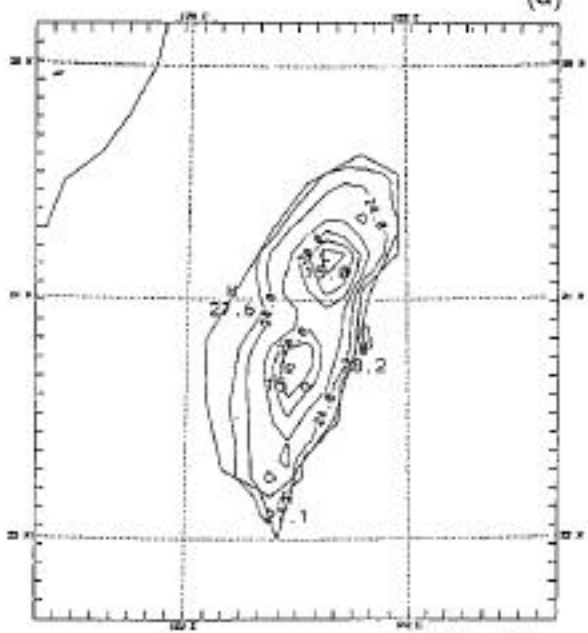


Fig. 8

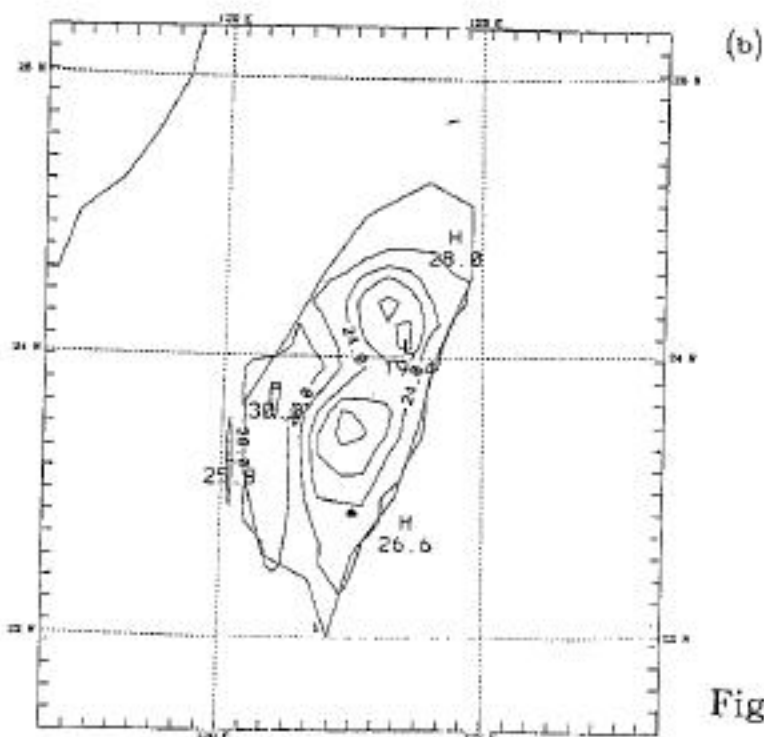
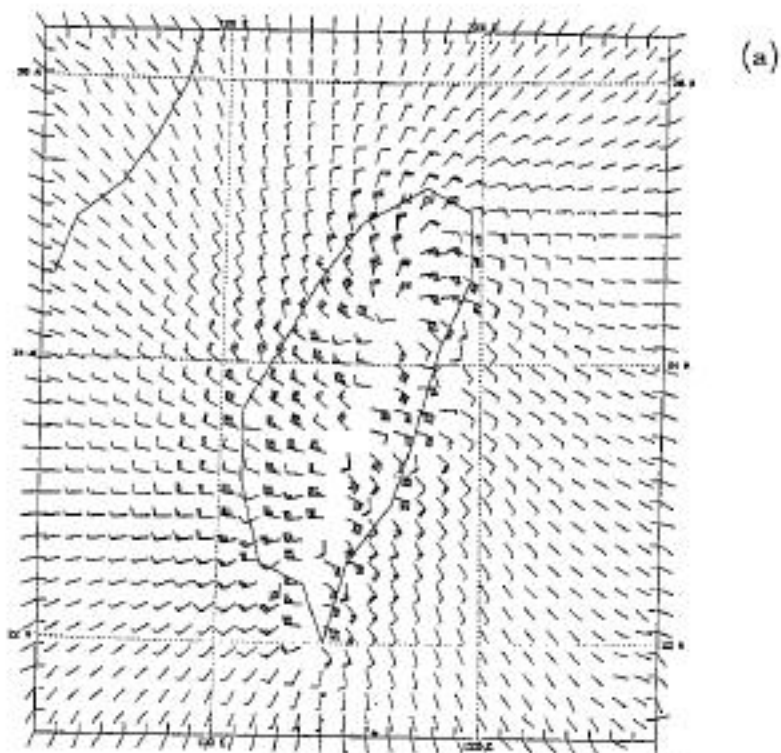


Fig. 9

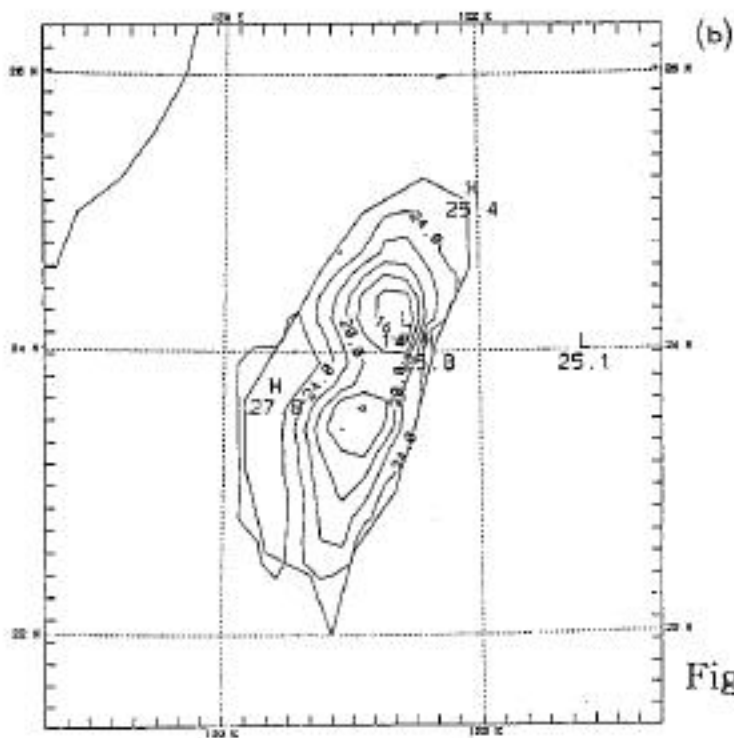
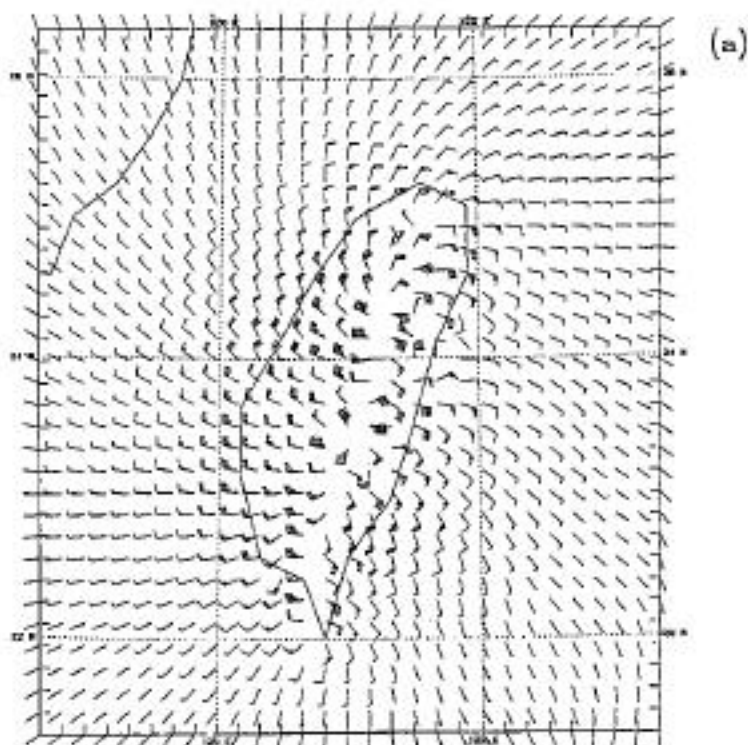


Fig. 10

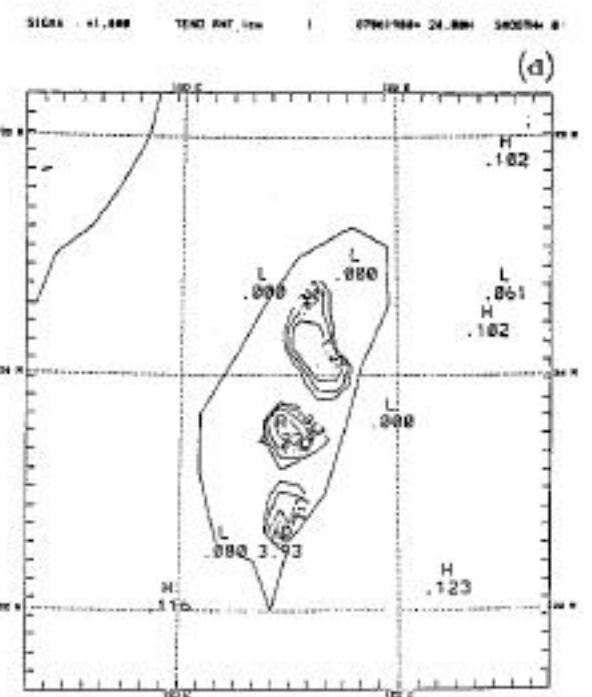
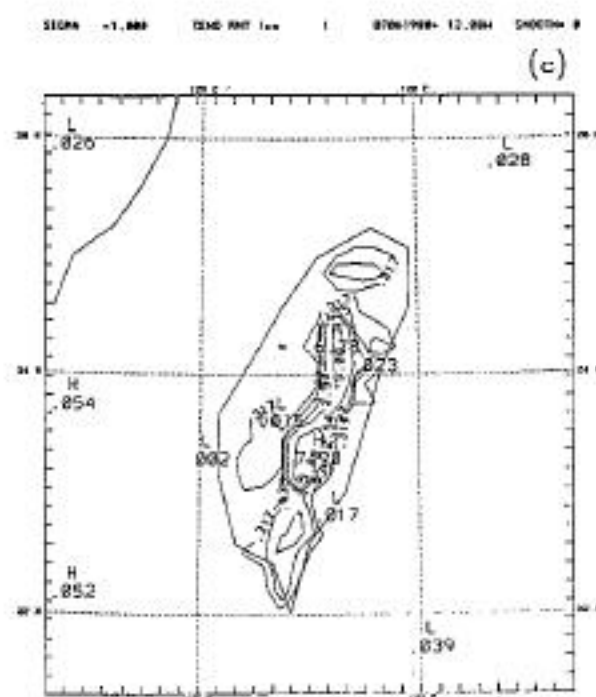
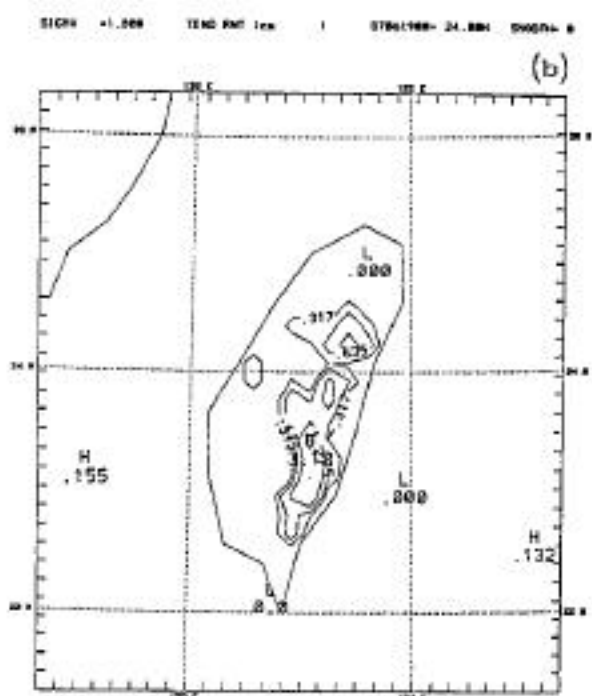
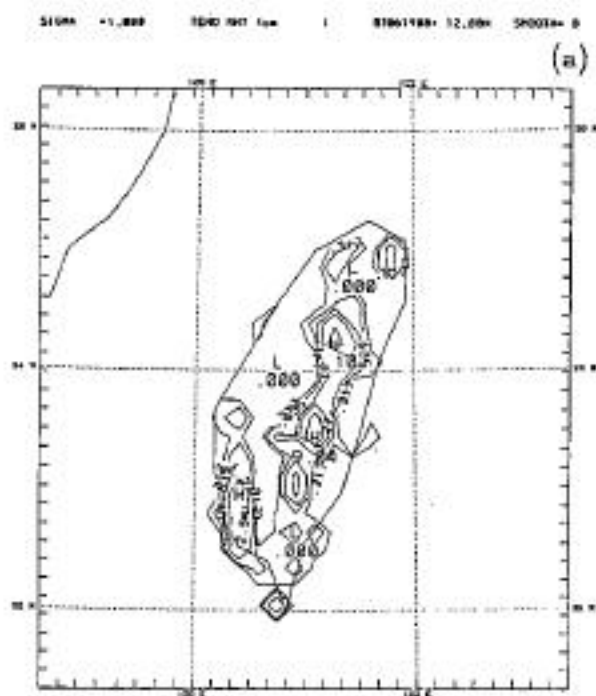
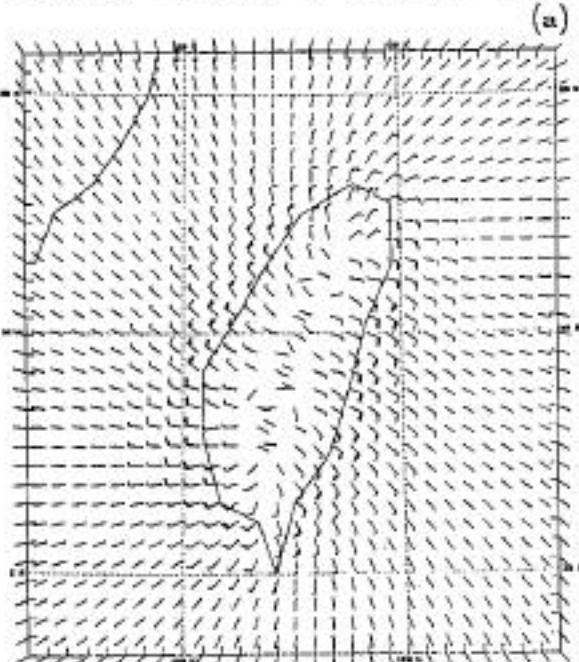
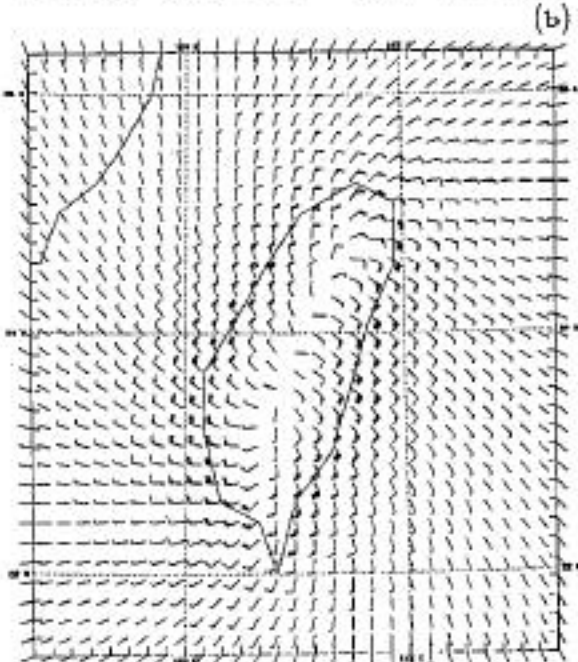


Fig. 11

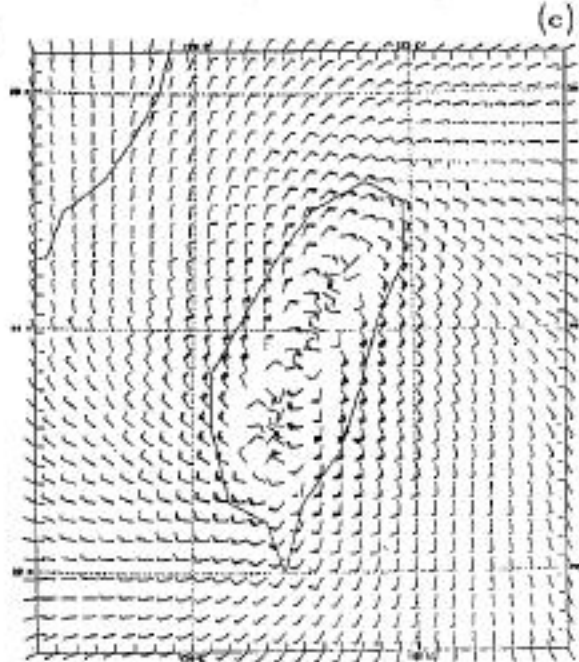
SIGMA = 0.795 DASH OF 1000'S | 07001980 = 1.000 DASH OF 0



SIGMA = 0.795 DASH OF 1000'S | 07001980 = 1.000 DASH OF 0



SIGMA = 0.795 DASH OF 1000'S | 07001980 = 12.000 DASH OF 0



SIGMA = 0.795 DASH OF 1000'S | 07001980 = 21.000 DASH OF 0

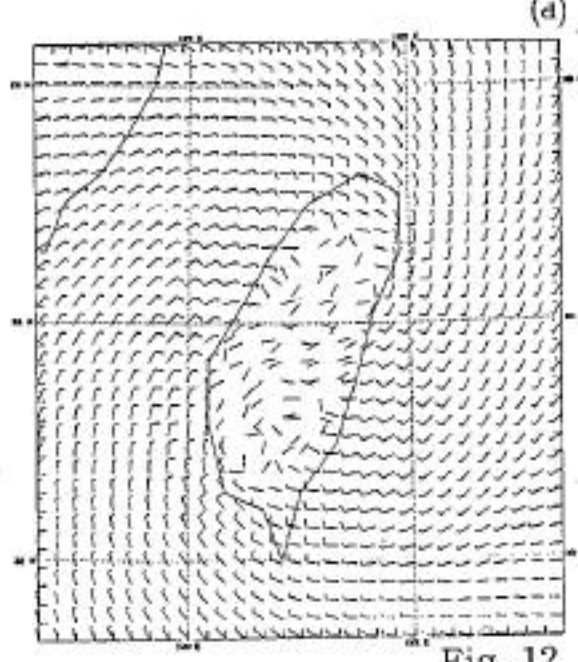


Fig. 12

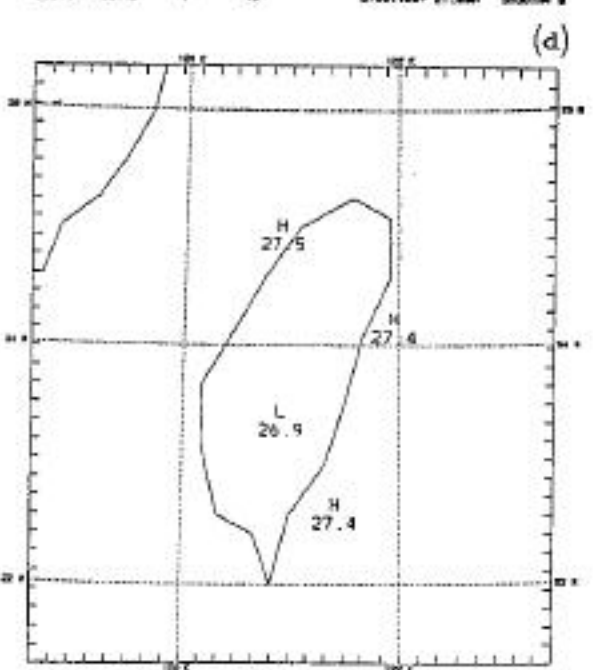
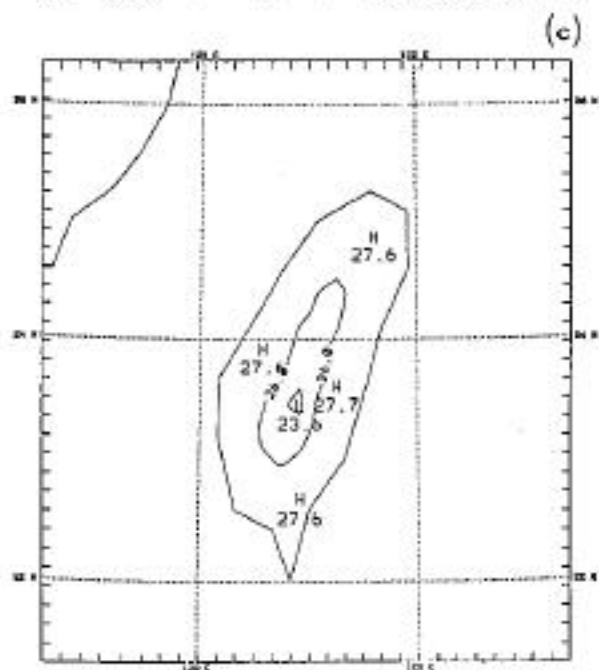
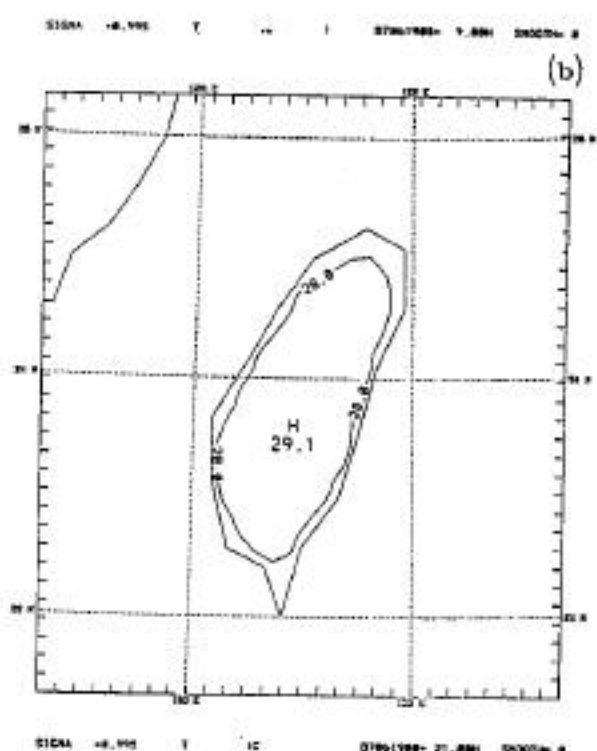
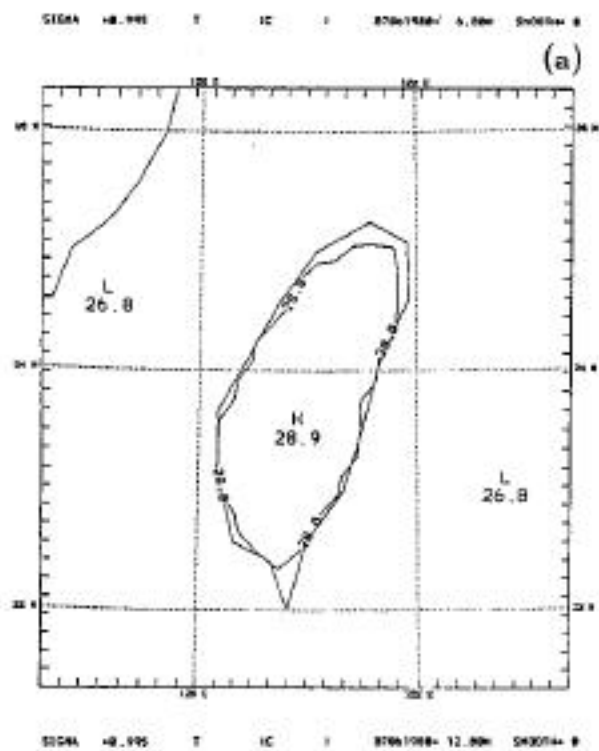
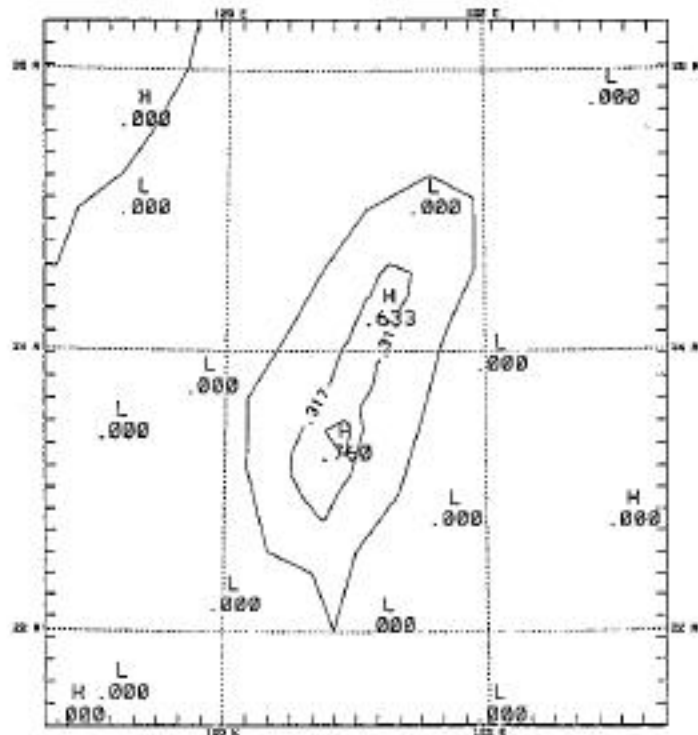
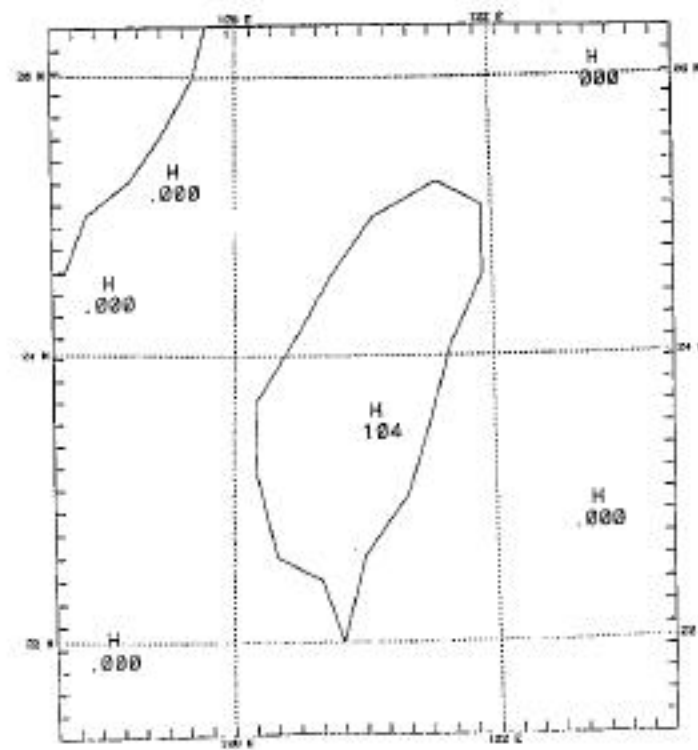


Fig. 13



(a)



(b)

Fig. 14

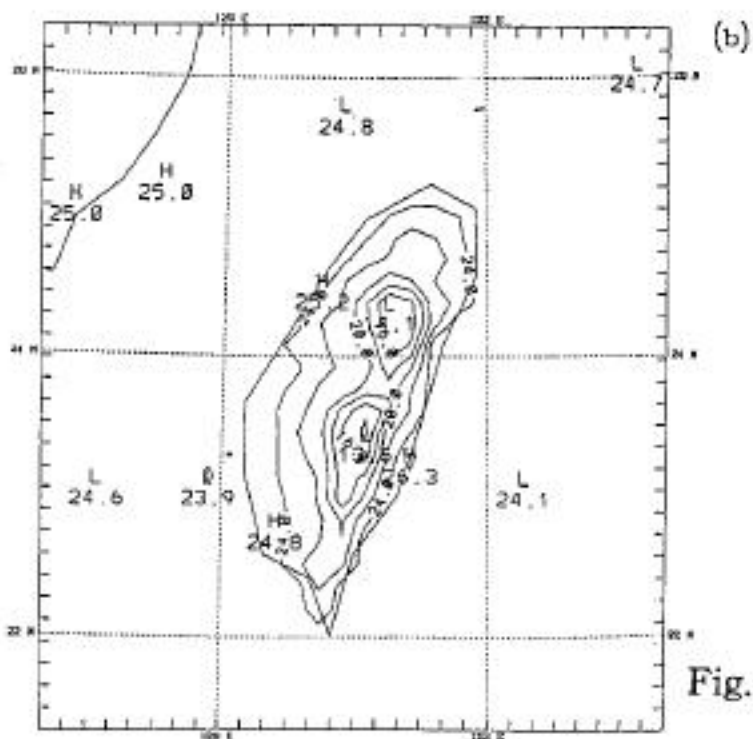
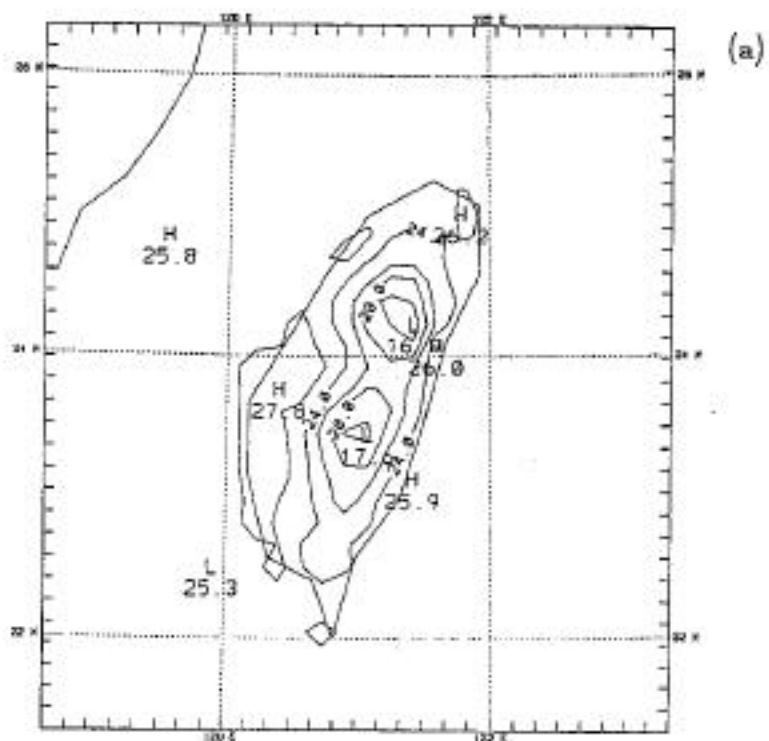


Fig. 15

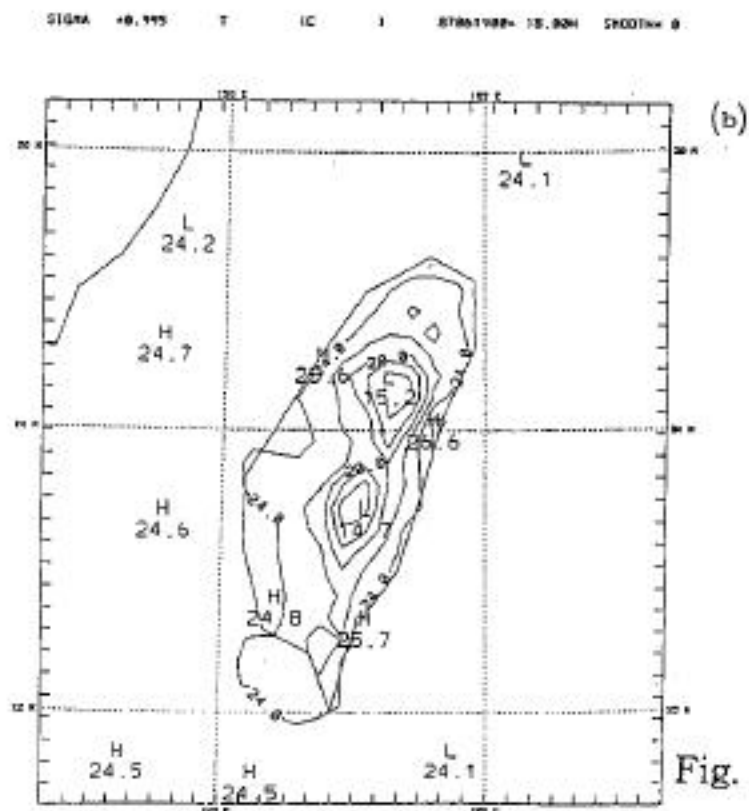
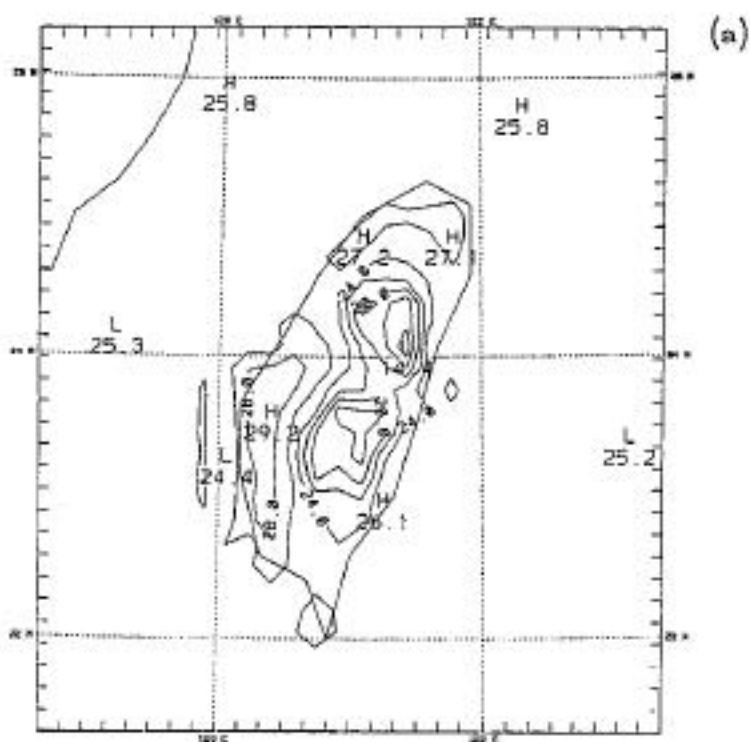


Fig. 17

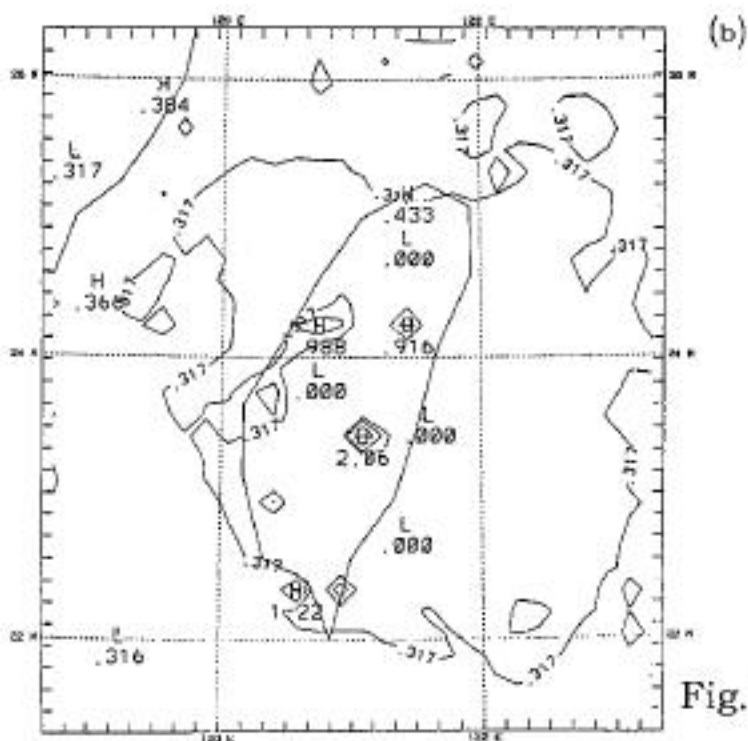
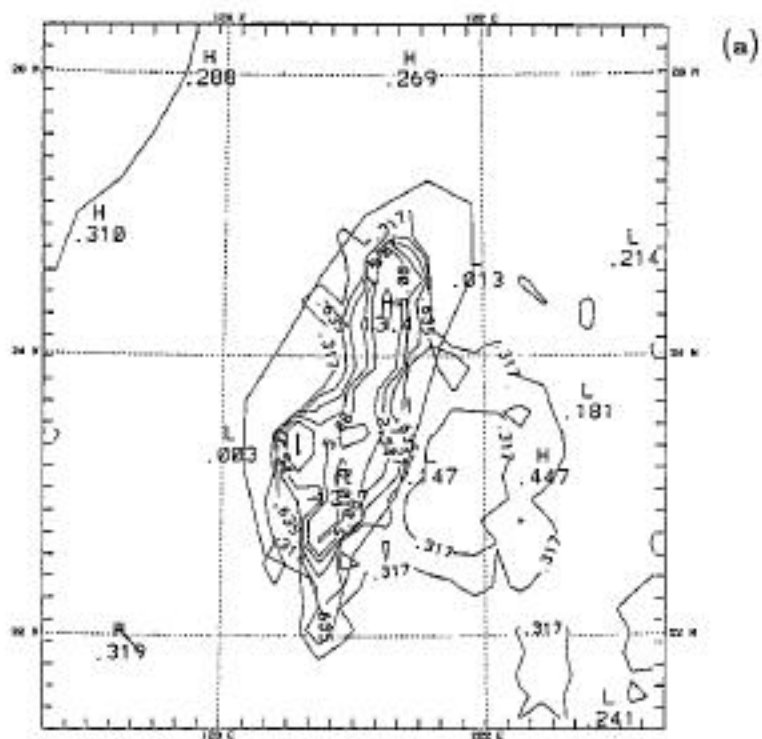


Fig. 18

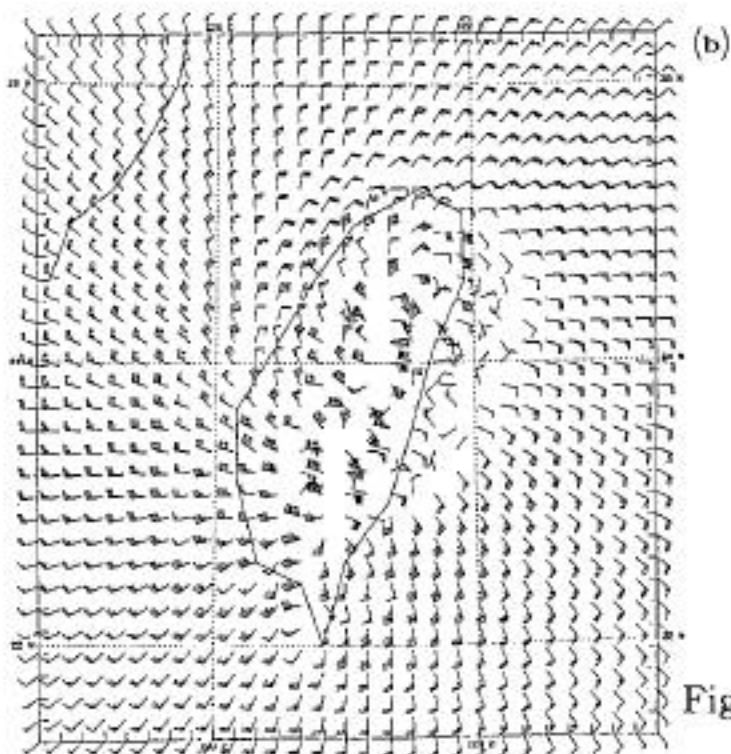
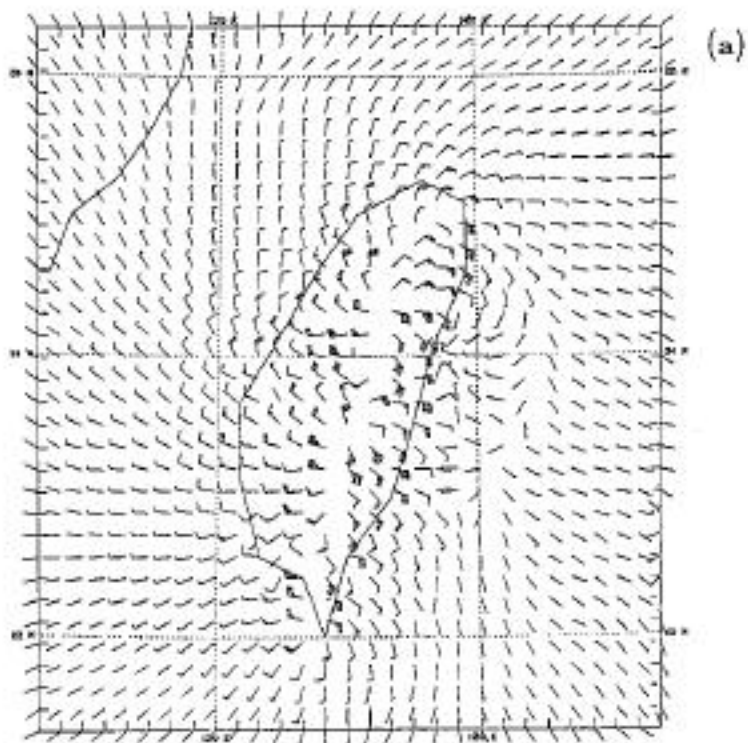


Fig. 19

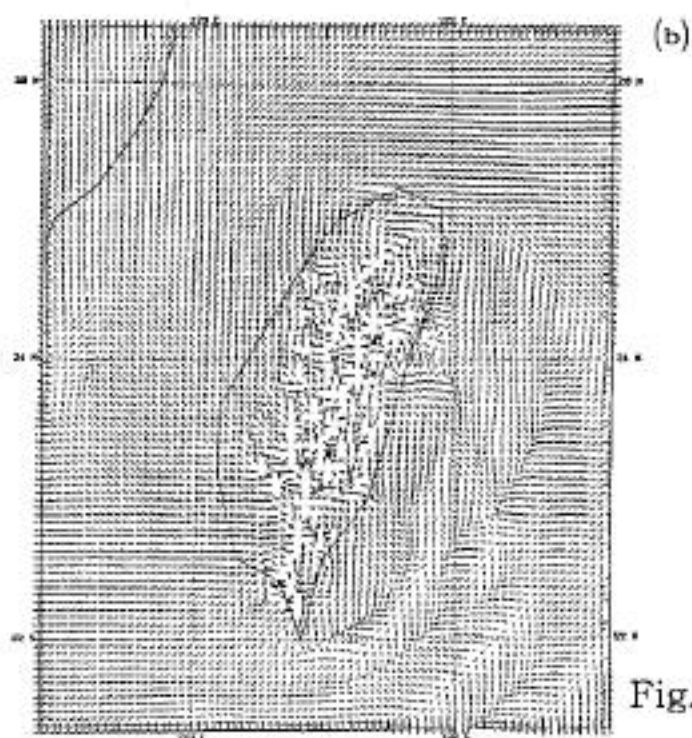
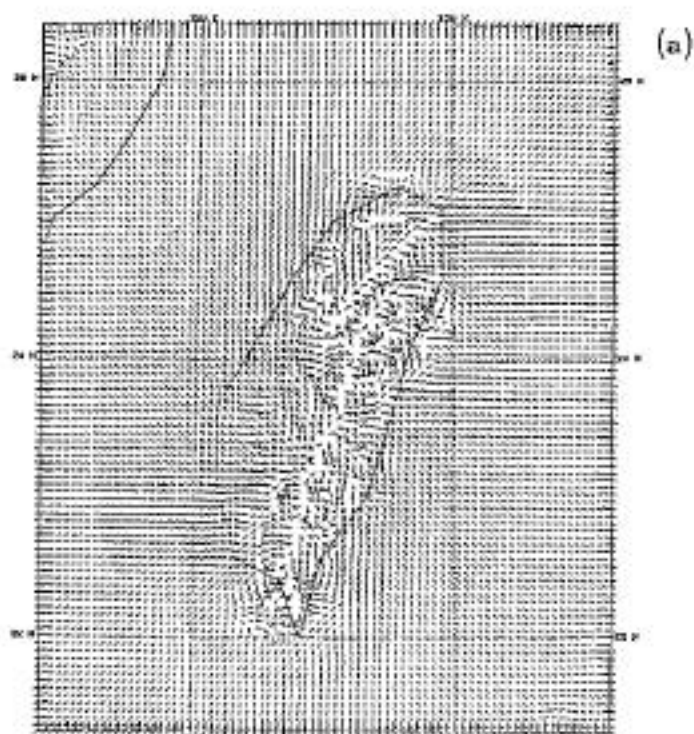


Fig. 21

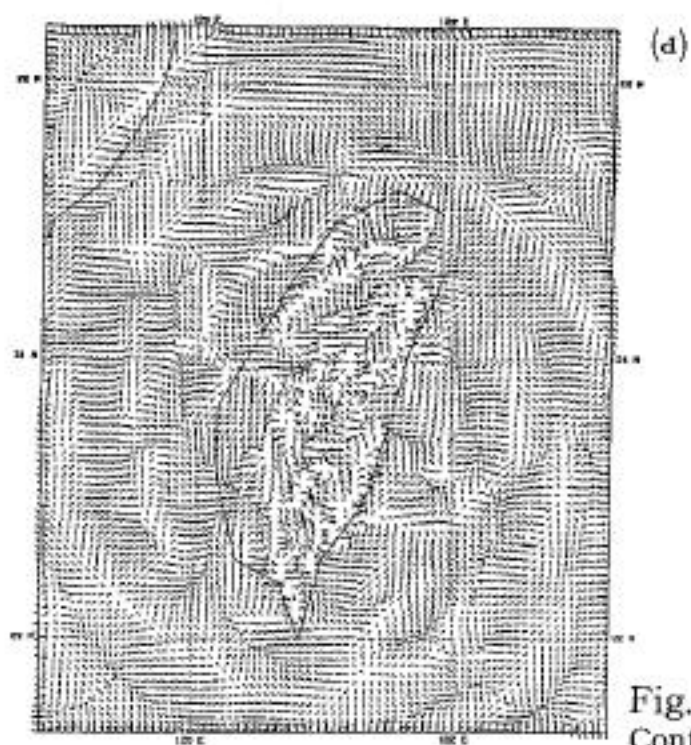
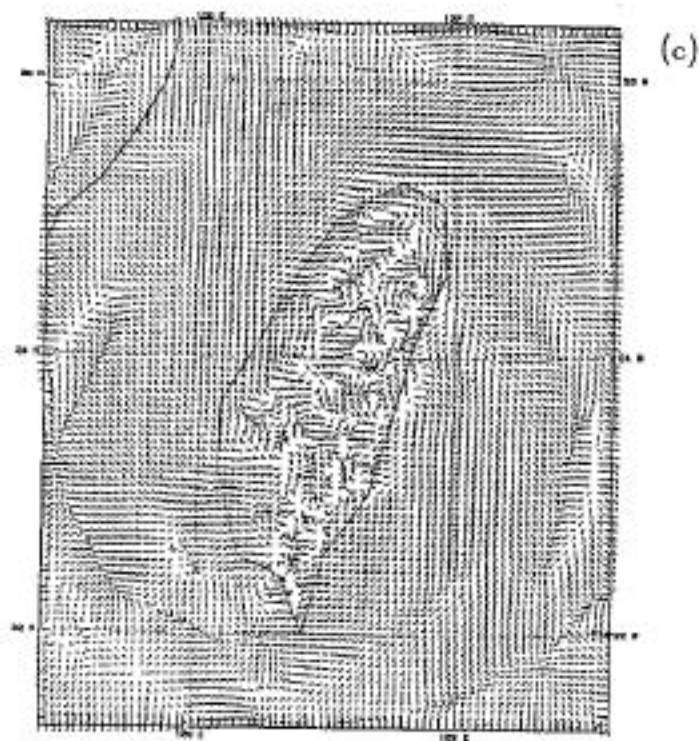


Fig. 21
Continued

SIGMA = 1.000 TEND RMT 1000 1 07001000+ 12.00H 5000TH= 0

